RSC Advances

REVIEW

View Article Online
View Journal | View Issue

Cite this: *RSC Adv.*, 2024, **14**, 3447

Advances in boron nitride-based nanomaterials for environmental remediation and water splitting: a review

Vishal Gadore, Soumya Ranjan Mishra, Ashish Kumar Singh and Md. Ahmaruzzaman *

Boron nitride has gained wide-spread attention globally owing to its outstanding characteristics, such as a large surface area, high thermal resistivity, great mechanical strength, low density, and corrosion resistance. This review compiles state-of-the-art synthesis techniques, including mechanical exfoliation, chemical exfoliation, chemical vapour deposition (CVD), and green synthesis for the fabrication of hexagonal boron nitride and its composites, their structural and chemical properties, and their applications in hydrogen production and environmental remediation. Additionally, the adsorptive and photocatalytic properties of boron nitride-based nanocomposites for the removal of heavy metals, dyes, and pharmaceuticals from contaminated waters are discussed. Lastly, the scope of future research, including the facile synthesis and large-scale applicability of boron nitride-based nanomaterials for wastewater treatment, is presented. This review is expected to deliver preliminary knowledge of the present state and properties of boron nitride-based nanomaterials, encouraging the future study and development of these materials for their applications in various fields.

Received 6th December 2023
Accepted 5th January 2024

DOI: 10.1039/d3ra08323c

rsc.li/rsc-advances

1. Introduction

In today's world, boron nitride (BN) nanomaterials are the most popular, promising, and effective nanomaterials. BN is a compound with equal numbers of alternately linked boron and nitrogen atoms. Boron nitride was believed to be a type of synthetic material, but recently, it has also been found in natural minerals.[1] BN is a compound that exists in several forms, including a soft hexagonal (h-BN) form having sp^2 bonded layered configurations, which is similar to graphite; a hard cubic (c-BN) form, which is analogous to diamond; and an amorphous (a-BN) form with properties that are the same as those of amorphous carbon.[2,3] Because of their advantageous properties, including electrical insulation, high thermal conductivity, chemical inertness, and optical transparency, hexagonal boron nitride nanoparticles have attracted special attention. These characteristics make BN appealing as a material for various uses, including optical coatings, lubricants, and protective and advanced ceramic composites.[4] As shown in Fig. 1, the crystal structures of BNs are represented by the cubic boron nitride (c-BN) and hexagonal boron nitride (h-BN). The hardest form of BN is c-BN, which has high density and is similar to a diamond crystal lattice. It is the second hardest substance known to date. However, due to the lack of an easy route for the preparation of c-BN compared to h-BN, research on c-BN is limited. Similar to graphite, h-BN has a layered hexagonal structure comprising covalently bound B–N rings. It is frequently utilized as a thermally conductive substance and an electrical insulator because it is chemically and thermally stable. Several h-BN nanostructures, similar to carbon-based graphitic nanomaterials, are listed as nanowires, such as BN fullerene, BN nanotubes (BNNTs), and BN nanofibers.[5–8] These h-BN nanostructures exhibit unusual band gap structures and electrical capabilities. Therefore, they are among the top research interests.[9] This review concentrates on the current developments in h-BN nanostructure surface modification and applications.

As a remarkable heat conductor, h-BN has 600 W m^{-1} K^{-1} of thermal conductivity and a broad band gap that varies from 5.5 to 6.4 eV depending on nanostructures. Considering this, h-BN is well known as an electrical insulator.[10–14] h-BN has demonstrated a wide range of possible uses in electrocatalysts,[15] thermally conductive nanocomposites,[16–19] far ultraviolet light-emitting diodes,[20] field emitters, nano-dimensional electronic devices,[21] and polymer nanocomposites for severe environments.[22] Additionally, they are utilized in biological applications[23] such as orthopaedic implants,[24] biosensing,[25,26] medication, and gene delivery.[27,28] There is a lot of interest in the use of h-BN nanoparticles as functional fillers to reinforce and modify polymer materials. For instance, BNNT-polymer composites with high BNNT fractions were created by Zhi *et al.*[29] In this review, a variety of thermoplastics, including poly(ethylene vinyl alcohol), poly(methyl methacrylate),

Department of Chemistry, National Institute of Technology Silchar, 788010, Assam, India. E-mail: mda2002@gmail.com

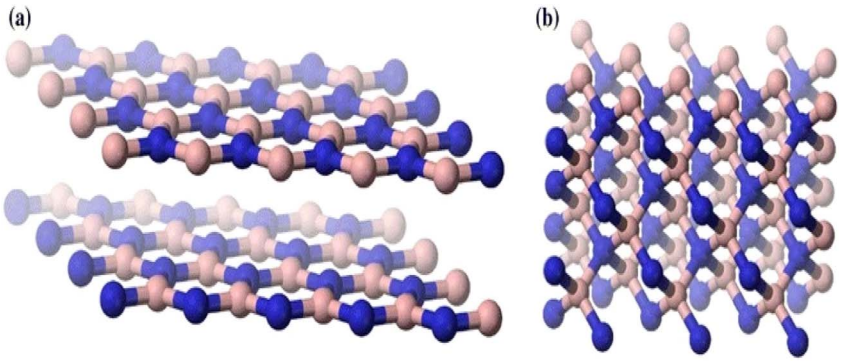

Fig. 1 Crystal form of (a) hexagonal boron nitride and (b) cubic boron nitride.[25]

poly(vinyl butyral), and polystyrene, were used as a matrix. By incorporating 20 wt% to 30 wt% of BNNTs into these polymers, the resulting polymer composites achieved up to twenty times the thermal properties of polymer nanocomposites, a break of an electric field that was 20% stronger, and a temperature expansion coefficient that was 20% lower.

To create dielectric epoxy composites with excellent thermal conductivity,[30] we used h-BN nanoparticles as fillers. A reduced dielectric loss factor with increased thermal conductivity of the nanocomposites demonstrated their promise for packaging and heat management in a micro-electronic gadget. Additionally, BNNF (boron nitride nanofiber)-strengthened polymer nanocomposites were created and researched. The BNNF/polymer composites, with 31.3 wt%, which show a superior in-plane heat conductivity of 60 W m^{-1} K^{-1}, were demonstrated by BNNF. This makes this composite a suitable alternative for thermal interface materials (TIMs) in heat management applications. A polymer composite with boron nitride nanosheets (BNNSs) demonstrated a notable reduction in CTE and an improvement in the elastic modulus[31] until the transparency of the composite films was nearly identical to that of the pure polymer films, demonstrating how they may be used in composite optical windows, optoelectronic devices, and other applications.

Even with these outstanding qualities and good uses, it is important to note that, similar to other nanomaterials, the high surface energy and significant tendency to agglomerate severely restrict the practical applications of h-BN nanoparticles. The disadvantage is problematic in composite applications due to low dispersion and surface characteristics. Most researchers concur that these two factors are crucial to the characteristics and application of polymer composites. Dissimilar graphite carbon nano-materials, whose interfacial and separation attributes may be easily tailored using a variety of covalent and non-covalent surface modification techniques, made the h-BN surface modification quite tricky. There are numerous hypotheses that explain this observation. Firstly, because of the electronegativity differences between boron and nitrogen, the covalent sp^2 links between the boron and nitrogen atoms are somewhat ionic, the same as the carbon–

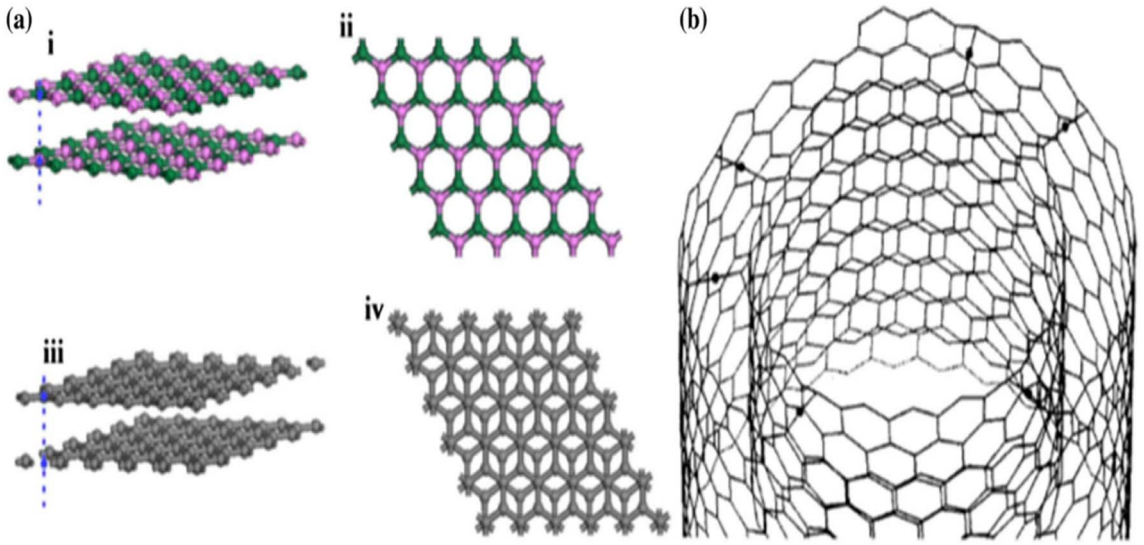

Fig. 2 (a) Morphology of (i) and (ii) h-BN sheets and (iii) and (iv) graphite sheets showing differences in the order in which they are stacked.[31] (b) Interaction between the neighbouring layers of a multi-walled nanotube.[32]

carbon bonds in a graphitic structure, which strengthens the boron-nitrogen connections and makes them harder to separate. Secondarily, the difficulties in the surface modification of h-BNs are also due to the unique stacking order of the atomic surface, shown in Fig. 2a.[31] More crystalline graphite causes a Bernal (AB) stacking sequence, at which the atomic plane is moved to half hexagon [Fig. 2a(i) and (ii)]. In h-BN, the adjoining planes, hexagons are superimposed, similar to how they are stacked in AA′; thus, the B atoms are stacked on top of and below the equivalent N atoms in h-BN [Fig. 2a(iii) and (iv)]. These characteristics may cause a "lip–lip" interaction between the nearby BN surfaces, as seen in Fig. 2b (for the sake of clarity, only the constructions made of nanotubes are displayed here; this phenomenon also occurs in other nanostructures, such as nanosheets).[32] Bridges are then created by the chemical bonds that occur between the atoms of boron and nitrogen in the nearby layers. In conclusion, h-BNs are more resistant to chemical modification than graphitic materials because of their greater chemical inertness. The new material features of h-BN now make it an intriguing material in its own right, enabling a wide range of optical,[20,33,34] electro-optical,[35,36] and quantum optics[37] functions.

By creating hyperbolic phonon polaritons in a natural material, its extremely anisotropic crystal structure, characteristics, and polar chemical bonding may be used in device applications in IR nanophotonics.[33,34] Even at ambient temperature, its point defects, which have single-photon emission characteristics, can produce quantum emitters in the visible to the near-IR region.[37] In order to fully utilize h-BN for electronic usage, techniques for manufacturing and preparation must be advanced, encompassing thin-film and bulk crystal formation device integration, metallization, etching, and deposition. The potential for several of these emerging applications was significantly enhanced by significant advances in producing bulk, good-quality, isotopically nourishing materials.[38,39] These initiatives are currently in the beginning stages. However, improvements in mass growth,[40] chemical vapour deposition (CVD),[41] and molecular beam epitaxy (MBE)[42,43] have been observed.

Although various existing review articles discuss the applications of BN nanotubes, the present review article aims to provide comprehensive information on BN nanostructures. For the first time, the present state-of-the-art review summarizes the structural properties of BN, its synthesis, development, modifications and potential applications in the field of environmental remediation and energy production. The scope of the suture research is also discussed to promote further research on the topic.

2. Properties and structure of BN

A highly anisotropic crystal of boron and nitrogen atoms is tightly bound in the in-plane direction, known as hexagonal boron nitride.[44] The B–N bond is polar covalent because the electronegativity difference between nitrogen and boron is more than 0.4 eV. Only van der Waals bonds exist between neighbouring sheets when the sheets are out of the plane, as in the case of graphite.[45] Despite having an energy gap of about 6 eV, h-BN is an indirect bandgap semiconductor with a very high internal quantum efficiency for strong ultraviolet emission (up to 40%). Because of the high anisotropic crystal structure of h-BN, the frequencies of the typical lattice vibrational modes (optic phonons), which have two different branches, are likewise highly anisotropic. These are termed upper ($\lambda_{FS} \approx 6.2$–7.3 μm) and lower ($\lambda_{FS} \approx 12.2$–$13.1$ μm) bands, where λ_{FS} stands for the wavelengths in free space, and they are developed from in-plane and out-of-plane phonons respectively. Each branch's longitudinal optic and transverse optic phonons were spectrally separated because of the polar nature, creating a highly reflecting "Reststrahlen band".[46] Surface phonon polaritons are possible in this band, with the optic and acoustic phonons generating a phonon sideband in the ultraviolet luminescence spectrum.

Hassel[47] and Brager's[48] recognized theory for BN is that it has a graphite-like arrangement with B and N atoms replacing the carbon atoms, and has been assigned structural type B.12 in the "Struckturbericht".[49] The observed and computed intensities do not correspond well with this structure, but a thorough re-evaluation has been done, as the original work is susceptible to additional criticism. Hence, the conclusion is that the Hassel structure is wrong.

Copper and manganese K-radiation were used to produce powder photographs of the crystalline structure of BN. There were lines found that corresponded to 28 diffraction planes, or these may all be classified based on a hexagonal unit cell with dimensions at 35.5 °C of $a = 2.50380 \pm 0.0001$ A, $c = 6.6600 \pm 0.001$ A. A calibrated microphotometer and a Geiger counter spectrometer were both used to obtain intensity readings from the photographs. It is clear from these findings and the density that the layer structure of BN has an interlayer gap of 1/2 c; every layer comprises a flat network of B_3N_3 hexagons. Four possible arrangements of these layers satisfy the symmetry of a unit cell. Three of these methods involve distinct arrangements of B and N atoms among the carbon atom-occupied positions for graphite. The model that Hassel and Brager chose most closely matches the measured intensities, as shown in Fig. 3 and 4, and presents the fourth way. This is a novel form of packing where the locations of the boron and nitrogen atoms are switched in the neighbouring layers, and the hexagonal rings are placed right on top of one another. A comparison of the calculated and observed intensity demonstrates that BN has a novel form of packing, and not the graphite type. A most striking result of this distinction between the packing of BN and graphite is the variation in the relative strengths of the hkl lines when $h + 2k \neq 3n$. These lines become stronger when l is even and weaker when l is odd in BN. However, the opposite is true in graphite. This discrepancy is clearly evident in the powder images and cannot be explained by the carbon atoms' different atomic scattering strengths compared to B and N atoms.

The structural characteristics of various nanotubes are examined using theoretical and experimental means. Using molecular dynamics techniques and considering the interatomic interactions, theoretical simulations of structures were created. The Tersoff interaction potentials[50] suggested for BN

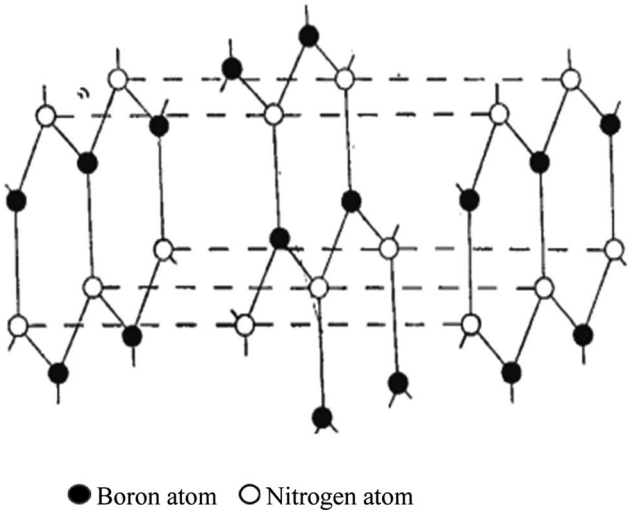

Fig. 3 Hassel structure of BN.[47]

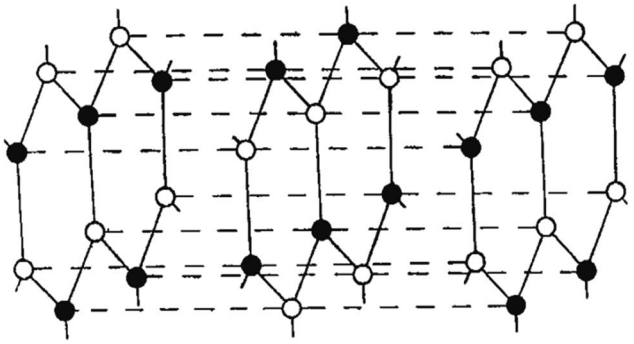

Fig. 4 Newly suggested BN structure.[47]

were used to define the structures.[25] The LAMMPS software[51] was used to carry out the simulation, and the Ovito[52] and VMD[53] programs were used to display the simulation results. These samples' (nanotubes) thicknesses ranged between 20 to 200 nm. Defocussing occurred on the range of many tens of nano-meters during electron microscope investigation (30–100 nm). These nanotube samples were generated in a gasostat using a graphite furnace for electron microscopy research.[54] An h-BN crucible was used to hold a sample of Yttrium Aluminum Garnet (YAG), which was then heated at a high temperature. The mp of YAG is 1942 °C. The raw powders contained in a tantalum ampoule were sintered to create the YAG sample in a high-pressure solid container.

2.1. Singlewall nanotubes

The best carbon nanotubes are cylindrical in form; for these materials, the idea of chirality has been proposed. Chirality is defined by two integers (m, n) representing the position of the network hexagons that must line up with the hexagons at the origin of the coordinate as a consequence of the network convolution.[55]

Under this context, tubes were divided into three categories: "zigzag" configurations (m, 0), "armchair" configurations (m, $n = m$), and "chiral" configurations (m, $n \neq m$). The single-wall nanotube diameter may be calculated using chirality indices.

$$D = \sqrt{3}d\frac{\sqrt{3}d_0}{\pi}\sqrt{m^2 + mn + n^2} \quad (1)$$

where d_0 refers to the gap between atoms in the hexagonal lattice that are next to one another. This value for BN is 0.145 nm.

Fig. 5 depicts BN nanotubes with various chiralities. The ideally cylindrical nanotube having smooth walls (a feature of carbon nanotubes) was reportedly predicted. However, the minimization of energy in the BN nanotubes results in the development of distinctive "ribbed" walls (Fig. 5). Nitrogen atoms are moved outward in the tube, while boron atoms are pushed inward. The simulation shows that the B–N bond length may vary between 1.5 + 0.1 Å for tubes with various chiralities. Electron diffraction patterns were used to identify the chirality of the nanotubes.[57]

2.2. Multiwall nanotubes

Regarding the structure and layout, multiwall nanotubes are more diverse than single-wall ones.[56] Multiwall nanotubes of transverse structures and longitudinal structures strongly depend on their development. Different kinds of nanotubes

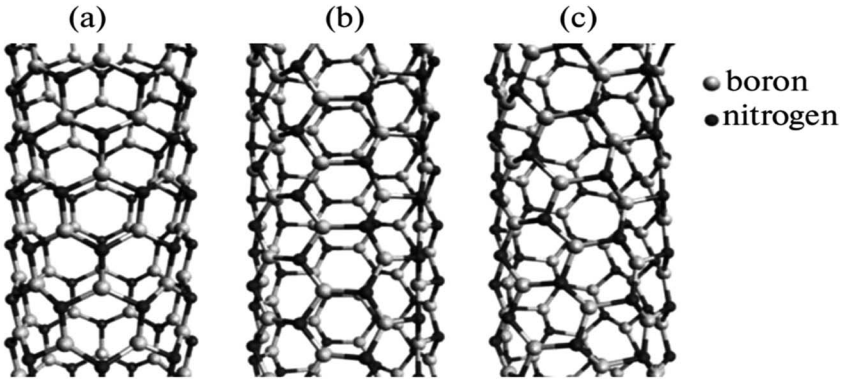

Fig. 5 Simulation of various chiralities in BN nanotubes: (a) zigzag, (b) armchair, and (c) chiral configurations.[56]

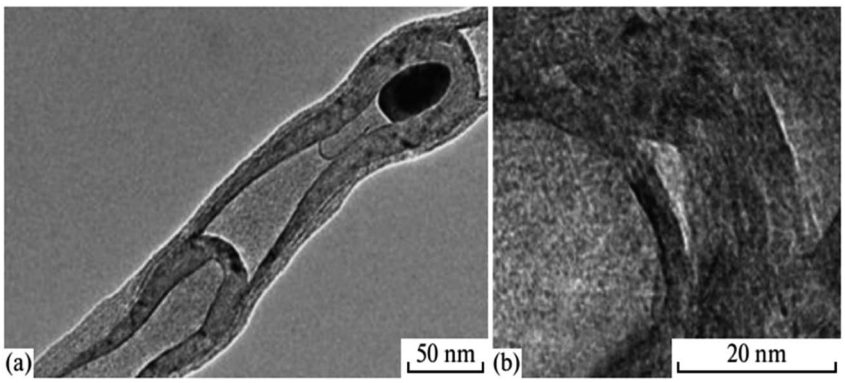

Fig. 6 (a) TEM image and (b) HRTEM image of a bamboo-like nanotube.[56]

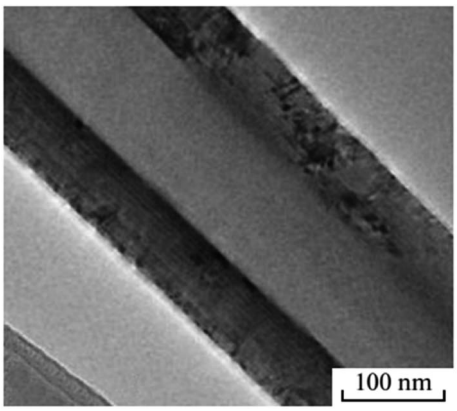

Fig. 7 TEM image of a multiwall BN nanotube.[56]

may result from synthesis.[58] Like carbon nanotubes, hexagonal BN nanotubes have an array of hexagonal networks arranged ideally below one another (as opposed to a graphite structure), with the B and N atoms alternately arranged throughout the *Z* axis. The two forms of nanotubes we typically saw were regular linear tubes and so-called bamboo-like tubes. The latter are frequently paired with defective ones, and their potential uses are not considered. However, it was demonstrated in ref. 59 and 60 that these nanotubes can be more advantageous than traditional, unstrained BN nanotubes in several applications. In contrast to regular tubes, bamboo-like ones are frequently twisted and interlaced. Their width range varies between 40 and 100 nm. A few tubes are filled, while others are empty (Fig. 6a). The curvaceous bands in the nanotube tips may be seen in the strong-resolution TEM images (Fig. 6b).

A multiwall BN nanotube is seen in Fig. 7. In experiments, nanotubes with 50–60 walls have often been seen. However, there are also specific tubes with 30 to 90 walls. As the number of walls increases, the shape deviates more from the ideal cylindrical shape. The interplanar distance may vary based on the perturbing impact on adjacent tubes. Thus, in multiwall BN nanotubes, many phenomena are present. EELS and element mapping were used to investigate the chemistry make-up of nanotubes. The nanotubes under review were demonstrated to contain a BN core covered in a carbon coating.[56]

Faceting causes the twisting of nanotubes. Additionally, the chance of discovering a rhombohedral BN interlayer increases with the number of walls inside a nanotube. Fig. 8 displays three nanotubes with a variety of walls: 2, 4, and 10 walls, respectively. The density of irregularities in packing various walls increases with the number of walls. For a simulated 10-wall nanotube, the beginning of faceting can be seen clearly.

3. Synthesis of BN

The development of h-BNs is crucial for surface modification. This is because structural elements, including the diameter, purity level, faults, and edge structure of BN, significantly impact the surface modification of h-BNs, which have an immediate connection to the synthesis procedures. This article

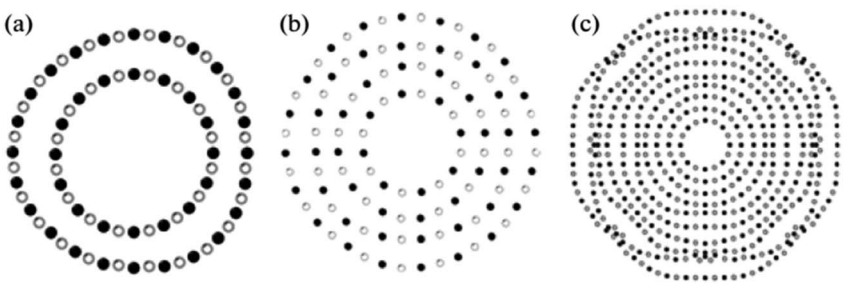

Fig. 8 Simulation of (a) two, (b) four, and (c) ten-walled BN nanotubes.[61]

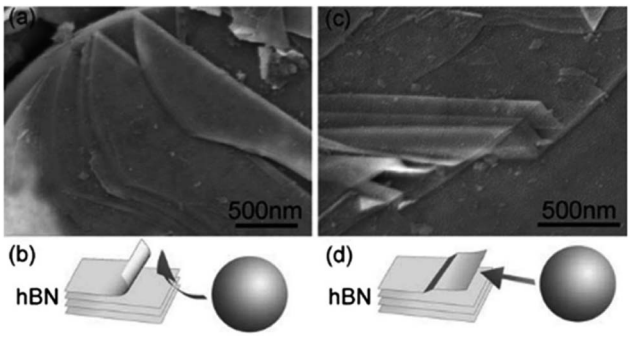

Fig. 9 SEM images illustrating the mechanism of mechanical exfoliation; (a) and (b) cleavage at the edge of h-BN nanoparticles, and (c) and (d) peeling of h-BN thin sheets by ball milling.[65]

briefly describes a few typical synthesis techniques for various h-BN nanostructures.

3.1. Mechanical exfoliation

The mechanical exfoliation process is also defined as mechanical peeling or mechanical cracking. Initially, sticky tapes were employed to separate graphene monolayers using this method.[62] By using this method, layer h-BNs may also be synthesized, and very thin sheets of h-BNs were achieved.[63,64] It could not maintain the van der Waals link between the adjacent h-BN layers by applying direct peeling force to the adhesive tapes throughout mechanical exfoliation. Still, the robust covalent boron–nitrogen bond structures remained intact and were detected using an optical microscope. Unfortunately, this method is not particularly effective for h-BNs due to the previously noted lip–lip interactions between the BN surfaces.[32] The shear force was also used to exfoliate h-BNs mechanically instead of the direct peeling force. The production of high-quality BNNSs from ball-milling h-BN powders in an N_2 environment was reported by Li *et al.*[65] They adjusted the ball-milling parameters to produce a mild shear force. Fig. 9 shows the SEM images of peeled h-BNs, and a suggested exfoliation pathway under a shear force that occurs in response to the milling balls.

3.2. Chemical exfoliation

It has been demonstrated that chemical exfoliation, the liquid exfoliation method, makes it straightforward to produce mono- and few-layer BNNSs that are almost devoid of redundant components like catalysts and might scale up to vast numbers.[66] Because of the strong interactions between polar solvent molecules and h-BNs, high polar solvents, including *N*,*N*-dimethylformamide (DMF), *N*-methyl-pyrrolidone (NMP), and isopropanol (IPA), were utilized to promote the synthesis of BNNSs. Large h-BNs might be divided into layered h-BNs by the cooperative action of sonication and a polar solvent. We produced pure BNNSs in thicknesses between 2 and 10 nm at the milligram scale.

3.3. Chemical vapor deposition (CVD) synthesis

Chemical vapour deposition (CVD) is applied to create excellent quality and good-performance thin film nanoparticles. In a basic CVD procedure, one or many more volatile preparations are exposed to the surface, and they react with or degrade on the foundation surface to generate the desired deposit. Lourie *et al.*[67] initially used the CVD process to generate BNNTs. They used borazine ($B_3H_6N_3$) as a precursor and Ni_2B molecules as a catalyst at 1110 °C in the synthesis of BNNTs. The SEM image of BNNTs is illustrated in Fig. 10. Since then, several h-BN nanostructures have also been created using CVD techniques. Significant advantages include the relatively low power input, excellent purity, and, most importantly, the extensibility of the CVD process. Currently, the CVD development of h-BN nanosheets mostly utilizes the pyrolysis of a single precursor, such as hexachloroborazine ($B_3N_3Cl_6$), borazine ($B_3H_6N_3$),[68] or trichloroborazine ($B_3N_3H_3Cl_3$),[69] or the combination of two compounds as the base material, like BCl_3–NH_3, BF_3–NH_3, and B_2H_6–NH_3.[70] Two typical chemical reactions involving two substrates in one case (chemical reaction (2)) and one substrate in the other (chemical reaction (3)), respectively, are given below.

$$BF_3 + NH_3 \rightarrow \text{h-BN} + 3HF \quad (2)$$

$$(CIBNH)_3 + NI(111) \rightarrow \text{h-BN/Ni(111)} + 3(HCL) \quad (3)$$

here, Ni(111) was the substrate for deposition. Beyond Ni(111), various transition metal surfaces, such as Ru(001), Pd(111), Pt(111), and Ni(755), that have similar lattice morphology with h-BN can also be used as substrates.[69] Ahmad *et al.*[71] produced high-quality h-BN nanowires using a straightforward CVD process at 1200 °C throughout a 30-minute growth period.

3.4. Other synthesis techniques

In addition to the methods already described, several methods have been investigated to create h-BN nanomaterials. Among

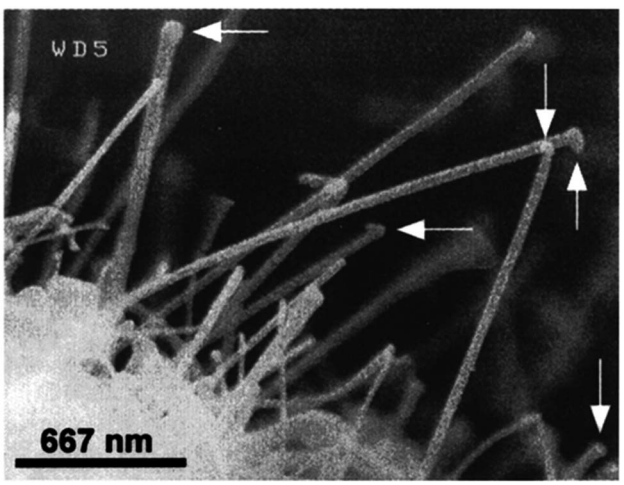

Fig. 10 SEM images of h-BN nanotubes.[67]

them are laser ablation,[72–74] plasma-arc technique,[75,76] and plasma-enhanced pulsed laser deposition.[77] The investigations for all of these methods, which often demand significant input energy (>2000 °C), are not as comprehensive as those for the earlier techniques.

A chemical reaction known as a substitution reaction occurs when an atom or functional group replaces one in a chemical molecule.[25] Han *et al.* used graphene sheets as templates to create extremely crystalline h-BN utilizing a carbon substitution process.[78,79]

$$B_2O_2(g) + 3C(sheets) + N(g) \rightarrow 2h\text{-}BN(sheets) + 3CO(g) \quad (4)$$

They put B_2O_3 powders in an open furnace, and coated them with graphene sheets and molybdenum oxide (as a booster). For 30 minutes, the furnace was kept at 1650 °C in a flowing N_2 environment. The residual carbon layers were then removed by gathering the product and heating it in the air. Using electrospun polyacrylonitrile fiber as templates, the widely utilized electrospinning method was employed to create constant BN nanofibers (BNNFs). By altering the electrospinning process parameters, such as the applied electrical field and B_2O_3 solution concentration, the diameter of the BNNFs may be adjusted.[7] The FE-SEM images of the BN nanosheets synthesized at 1200 °C are shown in Fig. 11.[80]

3.4.1. Green synthesis of BN. The green dry ice-assisted ball milling method prepared edge-functional two-dimensional composite nanosheets of BN. The heat performance of the BN aqueous nanofluids was first studied.[81] At a 5-vol% loading, we discovered that the BN aqueous nanofluids had a thermal conductivity of approximately 1.62 W m^{-1} K^{-1}. Fig. 12 depicts the conceptual layout of the covalently functionalized BN composite nanosheets. The conjugated π-system was not impacted by this technique, which added the COOH groups at the BN edges. The BN water nanofluids were generated by ultrasonically mixing the BN with distilled water for 30 minutes. It was generally known that BN's inherent hydrophobicity prevented it from dispersing in water. Fig. 12d shows that the liquid nanocomposite with a volume percentage BN nanostructure showed high water compatibility and a uniform black dispersion without evident macroscopic agglomeration. Surprisingly, after many months of storage, no precipitation

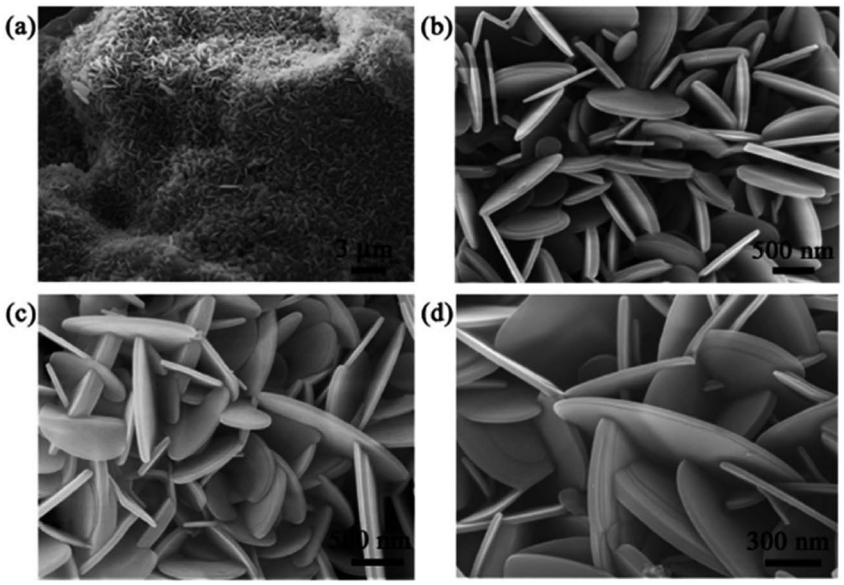

Fig. 11 (a) FE-SEM image and high-resolution FE-SEM images at (b and c) 500 nm and (d) 300 nm of BN nanosheets synthesized at 1200 °C.[80]

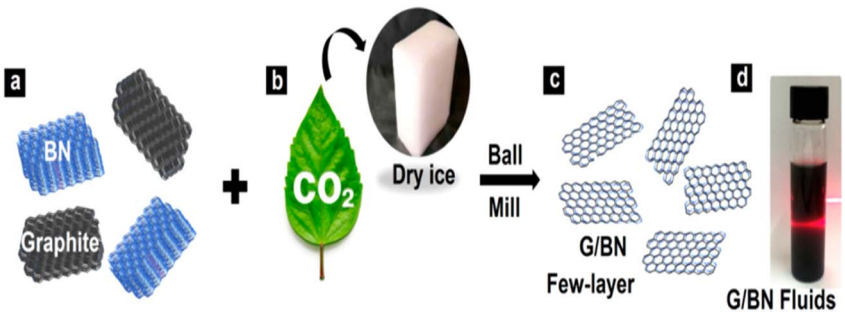

Fig. 12 G/BN schematic diagram.[83]

was seen, demonstrating the long-term stability of the BN–water nanofluids.[25] The significant improvement in the BN's dispersion in water is caused by the –COOH group's solubility at the BN's margins.[82] Analyses of the morphology and microstructure of the BN nanosheets were conducted using SEM and TEM. Few-layer nanosheets (usually fewer than ten layers) were made up of BN in the BN samples, and they could be clearly distinguished from their edges. Using TEM measurements that range from 0.1 to 0.8 μm, the lateral size of BN was measured.

4. Applications of BN and its nanocomposites

In various fields, including chemistry, metallurgy, high-temperature technology, electrotechnology, and electronics, h-BN has become well-established.[84] Their special qualities suggest numerous prospective applications in numerous technical sectors, including high mechanical stiffness, broadband gap, superior thermal conductivity, large surface area, and thermal stability. In particular, functional fillers made from h-BN nanoparticles have been employed extensively to create high-performance polymer nanocomposites.[25] The use of BNs and BN-based nanomaterials in prospective environmental applications like membrane separation, adsorption, and photocatalytic degradation to remove impurities has been thoroughly researched.[85,86] BN-based nanomaterials have been used in investigations on the surface assimilation of various inorganic (bulk metals), as well as organic pollutants (mainly dyes and medicines), and the information they provide can be useful when employing these materials to treat water and wastewater.[87]

4.1. Adsorption of pollutants

4.1.1. Heavy metals. Heavy metals are substances with a high density and low toxicity. Lead, iron, mercury, cadmium, zinc, arsenic, copper, and chromium are a few examples of heavy metals, and their actual volume is greater than 6 g m^{-3}.[88] Heavy metals enter the aquatic system through various pathways, and have environmental persistence and bio-accumulation characteristics. These heavy metals harm human health, as well as the quality of the underwater ecosystem.[89,90] According to Table 1, several inorganic pollutants were eliminated by utilizing various BNs, including BN nanosheets, BN nanoribbons, activated BNs, hexagonal BNs, and BN micro rods. The immediate removal of metal ions in solo and trio systems in simulated wastewater was used to examine the surface assimilation processes of Cu^{2+}, Cd^{2+}, and Ni^{2+} on BN.[91]

Adsorption in the solo adsorption process seems to occur very quickly (2 min), and with the following removal order: Cu^{2+} > Cd^{2+} > Ni^{2+}. However, the interaction of the metal ions in the ternary system causes variations in the adsorption performance. Cu^{2+} negatively impacted the elimination of Cd^{2+} and Ni^{2+}, whereas Cd^{2+} and Ni^{2+} were positively impacted by Cu^{2+}. These results point to a variety of adsorption processes, including the complex formation of metal ions with surface –NH_2 functional molecules,[92] ion interactions between metal ions and H of –OH,[93] and electrostatic interactions related to the pairings of –O and metal ions,[94] by incorporating a framework agent in the heat breakdown process of the activated BN substrate. It shows an exceptionally quick removal rate of 99.9 wt% (<6 h) and 90 wt% (<4 h) for different metal ions. It has an incredibly massive surface area (2100 m^2 g^{-1}) and a huge pore volume (1.66 cm^3 g^{-1}), effectively creating a new activated BN.[95] It unquestionably demonstrates that the greatest adsorption capabilities of excited BNs are significantly higher than those of penetrable BN and adsorbents carbon reported in early works.[96,97] It was found that excited BN with polar boron–nitrogen bonds exhibits considerably stronger positively attracting metal ions than excited carbon with covalent carbon–carbon bonds. This results from the rich electron density that

Table 1 An overview of BN-based nanomaterials' chemosorptive removal of several inorganic pollutants

BN-based nanomaterial	Species	Initial concentration (mg L^{-1})	Maximum adsorption capacity (mg g^{-1})	Ref.
BN	Cu^{2+}, Cd^{2+} & Ni^{2+}	10	18.42 ± 0.33, 12.00 ± 0.51 & 7.91 ± 0.57	91
Activated BN	Cr(III)	52	352	95
h-BN	Cu(II) & Ni(II)	300 to 700	200 & 95	98
Activated BN nanosheet	Hg, Cu & Pb	40	∼200 to 400	99
BN-nanoribbon	Cd & Cu	600 & 500	530 & 331	100
Porous BN-4 microrod	Cu	200	365	101
Fe_3O_4–BN	As(III) & As(V)	0.134 to 0.556 & 0.856	30.3 & 26.3	96 and 102
Polyaniline–h-BN	PO_4^{3-} & NO_3^-	100	106 & 67.9	103
g-C_3N_4/BCN	NaCl	500	13.6	104
Amine-functionalized porous BN	Cr(VI)	20	120.95	105
Diamide–pyridine-modified hierarchically porous boron nitride	U(VI)	100	87.5	106
P(AANa-*co*-AM)/BNNFs hydrogel	Pb^{2+}	300	490	107
h-BN–Fe_3O_4 nanocomposites	Cr(VI)	25	208.6	108
FeS@h-BN nanocomposites	U(VI) & Se(IV)	35 & 72	163.11 & 196.34	109
BCN–DAPhen	U(VI)	100	2050.8	110
Macroporous boron nitride fibers	Cd^{2+} & Zn^{2+}	350	2989 & 1885	111
Porous BN	Ni(II)	40	237.6	112

polyelectronic nitride allots to metal ions and the "lop-sided" density feature of ionic B–N bonding. The extensive surface area and abundant interspaces in the excited boron nitride significantly contribute to the material's high adsorption capacity and efficiency.[91]

With additional bulk metals, Pb^{2+} was efficiently removed utilizing a small layer of BN nanosheets fabricated employing a low-temperature manufacturing approach.[113] According to the results of interference testing, the adsorbents displayed a strong affinity for Pb^{2+} (845 mg g^{-1}), while being hindered by heavy metal ions like Cd^{2+}, Ni^{2+}, and Cu^{2+} ions (their adsorption capacities were 312, 201, and 402 mg g^{-1}, respectively). In order to explain the removal of Pb^{2+}, both chemical and physical adsorption processes were utilized. At pH = 6, the electrostatic interaction between the negatively charged BN adsorbents and the positively charged ions may be a major factor in the Pb^{2+} adsorption on BN nanosheets. The "lop-sided" density features of boron-nitrogen bonds form extra $-NH_2$ and B–OH bonds, showing that multi-electron nitrides might modify different electron densities on the metal ions. Therefore, the polarity of boron-nitrogen bonds was adequate for removing Pb^{2+}.[95] Overall, the large number of chemical linkages that form coordinate bonds with lead ions on the BN nanosheets are largely responsible for the high removal efficiency of lead ions, including the strong B–O–Pb interaction and $-NH_2$/Pb complexation.[114] Fig. 13a details the feasible mechanism of Pb^{2+} adsorption on BN nanosheets. Most earlier investigations on the removal of heavy metals utilizing various BNs have established that bulky metals were in opposite charge to manufactured BNs and might interact electrostatically, accelerating the adsorption response.[115–117]

4.1.2. Dye compounds. The available water is rapidly becoming polluted due to anthropogenic activities and growing industrialization.[118] Synthetic dyes that are widely utilized in various industries, including paint, food, tanneries, smelting, textiles, pulp and paper, cosmetics, and pharmaceuticals, are one of the main causes of pollution. Synthetic dyes have aromatic components and are often resistant to oxidizing chemicals, light, and heat.[119] They are also not biodegradable.[120] They damage aquatic life and make the water less transparent.[121,122] According to estimates, a dyeing process may result in the loss of 30% of the world's dye supply.[123] They are highly soluble in water, making them easily transportable to the environment and potentially dangerous to human health.[124] Because certain dyes are particularly poisonous, dye wastewater can cause cancer and mutation in people. It can also cause skin irritation, allergies, and dermatitis.[125,126]

Consequently, there is a pressing need to clean industrial effluent with dye contamination. Reverse osmosis,[127] advanced oxidation processes,[128] membrane filtration,[129] coagulation–flocculation,[130] and adsorption[131] are just a few of the methods that can be used to treat industrial wastewater. Adsorption is typically favoured among them because of its benefits, including cheap operating costs, greater efficiency, and an environmentally friendly nature.[132]

The study of methyl orange surface assimilation onto BN nanosheets included theoretical and experimental analysis.[133] The synthesized adsorbent has the greatest experimental adsorption capacity, 575 mg g^{-1}, which is attributable to the strong Coulomb interaction between the positively charged BN nanosheet and negatively charged methyl orange. Particularly, it was found that the chemical hardness, electrophilicity, and electronegativity data of the methyl orange–BN clusters are 1.45 eV, 5.51 eV, and 4 eV, respectively. The interaction between the adsorbent surface and the dye chemical is another important aspect of adsorption. According to research based on calculations using density functional theory, the oxygen atom of a methyl orange compound is closest to the BN nanosheet with

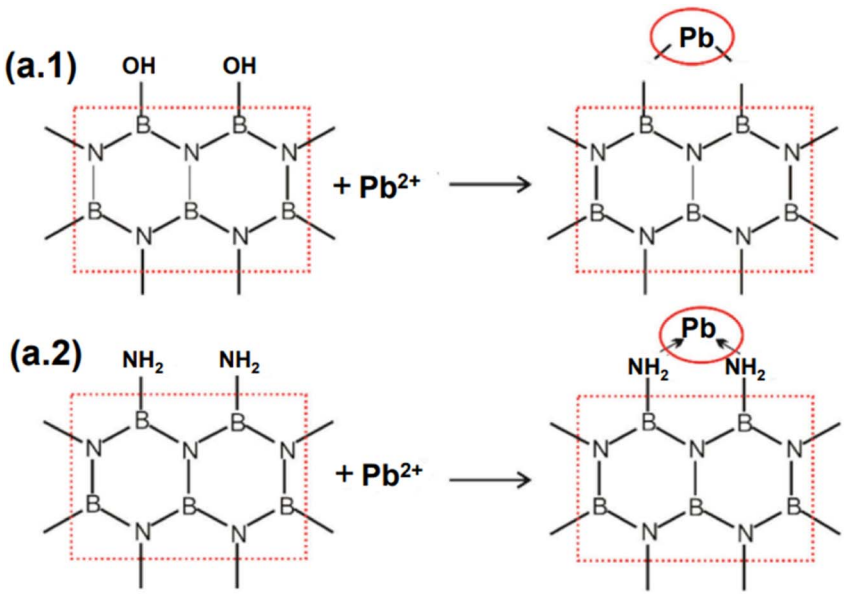

Fig. 13 The probable mechanisms of (a.1) B–OH & (a.2) $-NH_2$ in lead ion adsorption on the BN-550 nanostructure.[113]

a range of 0.233 nm. The desorption and reusability of BN nanosheets are allowed by the physical feature of methyl orange adsorption on BN nanosheets. The modified structure is symmetrical, and the reactions are exothermic, according to the measured adsorption energy of methyl orange, which looked to be −296 kJ mol^{-1}.

In a different investigation, negatively charged or activated BN fibres and the cationic dye methylene blue interacted electrostatically to reach the highest adsorption capacity of 392 mg g^{-1} at pH 8.0 and 30 °C.[134] Since the BN filament has a "lopsided" density feature of significant ionic boron-nitrogen bonding, and poly-electron nitrides have the potential to allocate a greater electron cloud to the positively charged solute, the polar boron–nitrogen bond is suitable for methylene blue chemical adsorption.[135] At pH levels higher than 2, the surface charge of the influenced BNs shifts toward a negative charge, which enhances the adsorption of the positively charged methylene blue. The penetrable BN, which has a massive pore volume of 0.63 cm^3 g^{-1} and a very large specific surface area of 1100 m^2 g^{-1}, enhances the adsorption performance.[136] Furthermore, additional activated sites in activated BN significantly improve the adsorption of methylene blue due to the abundance of hydroxyl and amino functional groups and the large density structural defects, which offer strong binding sites and enhance the dissociation of methylene blue on the BN fibres.[134]

A layered BN–carbon nitride nanocomposite was successfully made by calcining a combination of BN particles and urea (NH_2CONH_2) at an elevated temp of 600 °C, where urea is thermally polymerized through a calcination reaction to produce CN.[137] Using BN particles and urea as substrates. Fig. 14 depicts the expected creation process of the layered BN–carbon nitride nanoparticles. At starting concentrations of 220 mg L^{-1} and 120 mg L^{-1}, the BN carbon nitride nanocomposites successfully removed malachite green (1040 mg g^{-1}) and neutral red (1350 mg g^{-1}) from H_2O. Meanwhile, the anionic dyes MB (54.0 mg g^{-1}) and MO (55.9 mg g^{-1}) have comparatively poor adsorption capabilities. This finding suggests that neutral red withdrawal by the BN–carbon nitride nanocomposite may not be primarily caused by electrostatic attraction.

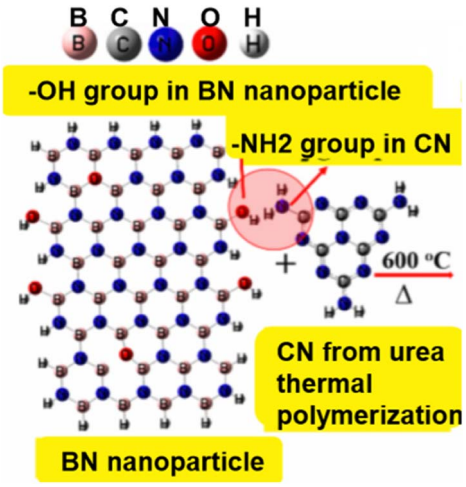

Fig. 14 The layered BN–carbon nitride composites (BN-30-600) are thought to be generated using urea and BN nanoparticles as precursors.[137]

According to a prior study, the size of the pollutants significantly affects how well adsorbents remove them.[138] In comparison to methylene blue (length = 1.42 nm and width = 0.54 nm) and methyl orange (length = 1.45 nm width = 0.43 nm), neutral red cationic dyes seem to have the lowest size (1.22 nm/0.49 nm). This is generally constant with their respective volumes of neutral red = 188 cm^3 mol^{-1}, methyl orange = 209 cm^3 mol^{-1}, and methylene blue = 207 cm^3 mol^{-1}. However, the size variance between these dyes is still insufficient to satisfactorily explain why neutral red's removal is around twenty times larger than that of methylene blue and methyl orange. The adsorption energy appears to have little impact on the removal of the adsorbent because the differences in adsorption energies between both the adsorbent and dye compounds (methylene blue = 35.2 kcal mol^{-1}, neutral red = 39.1 kcal mol^{-1}, methyl orange = 37.2 kcal mol^{-1}) are likewise negligible.[139] However, the biological neutral red molecules lack H^+ ions, and are difficult to break down in H_2O and precipitate in an alkaline medium. As a result, it was proven that neutral red might be eliminated by neutral red by attracting H^+. By using two additional cationic dyes (crystal violet and malachite green), the high affinity of BN-30-600 for H^+ has been verified.[137]

Using porous carbon–BN nano-scrolls resembling flower stamens, amazing dye surface assimilation capability was seen for eliminating methylene blue (250 mg g^{-1}) and Congo red (620 mg g^{-1}). The results were related to a variety of characteristics. Since pigments are filled in the cavities and adsorbed on the carbon–BN nano-scroll surface, their high surface area (890 m^2 g^{-1}) and porous structure are advantageous during the dye molecule's adsorption process. Following MB and Congo red adsorption, FE-SEM pictures reveal that the carbon–BN scroll feature was mostly unchanged. FTIR spectra show that the Congo red-coated carbon–BN with an aromatic benzene ring stretching band at around 1600 cm^{-1} is more powerful than the MB band.[140] We saw strong interactions between dye molecules and C–BN nanoscrolls. Raman and XPS investigations show that the C–BN molecule has sp^2 hybrid carbon and BN domains, resulting in conjugated π–π interactions with the dyes, including aromatic benzene (C_6H_6) rings. Furthermore, the B atom of carbon–BN interacts with a Lewis base through the nitrogen and sulfur atoms of Congo red and MB, creating Lewis-acids and Lewis-bases interactions.[141] Furthermore, negatively charged ionized boron–oxygen bonding enhances the hydrophilicity between carbon–BN and pigments, facilitating enhanced adsorbing behaviour and exciting cationic dye molecules like MB due to electrostatic interactions.[142] The summary of the adsorptive removal of dyes by BN-based nanomaterials is given in Table 2.

4.1.3. Pharmaceuticals. Antibiotics are frequently employed to manage illnesses in humans, animals, and plants due to their capacity to treat diseases brought on by infections.[157–159] However, a sizeable portion of these antibiotics

Table 2 An overview of the adsorptive removal of dyes by BN-based nanomaterials

BN-based nanomaterial	Dye compound	Initial concentration (mg L^{-1})	Maximum adsorption capacity (mg g^{-1})	Ref.
BN-based nanosheet	Methyl orange	110	575	133
h-BN	Rhodamine B & sunset yellow FCF	100 & 75	140 to 208 & 58 to 105	131
Polydopamine microspheres	Methylene blue	10	90.7	141
BN carbon nitride	Neutral red & malachite green	220 & 120	1350 and 1041	137
Activated BN	Congo red & methylene orange	50	300 & 400	95
h-BN	Methylene blue	500 to 200	230	143
h-BN whiskers	Rhodamine-B & methylene blue	3 & 60	210 & 13 973	144
Calcium alginate immobilized graphene oxide	Methylene blue	20 to 70	181.81	142
Ag–BN	Rhodamine-B	100	880	145
Porous BN	Methylene blue	10 to 50	189	146
Hexagonal boron nitride nanosheets	Methylene blue & acridine orange	10 to 500	415 & 286	147
BNNS–PVDF	Methylene blue	50	142.86	148
BNNS	Methylene blue	50 to 300	322.5	149
Porous BN	Congo red & methyl green	350 & 250	1096 & 1203	150
Cu–BNNS	Rhodamine B	500	743	151
Boron carbon nitride	Methyl blue & basic yellow-1	136.4 & 101.4	1220 & 560	152
Carbon-doped boron nitride	Sulfamethoxazole	10	28.75	153
BCN	Methylene blue	10 to 50	212.8	154
Oxygen-rich fish-scale-like porous boron nitride	Methylene blue	50	422.6	155
BNHSs with ultrathin shells	Basic yellow 1	40	191.7	156

is excreted into the environment since they are not utilized in metabolism. Therefore, it has been shown that they contaminate groundwater and surface water.[160,161] These can have a negative impact on human health by reducing immunity. By impacting smaller organisms like algae, they may potentially represent a danger to the ecological sustainability of the environment.[162] Because of this, removing antibiotic residue from wastewater at the source, including hospitals, households, and pharmaceutical industries, is crucial before releasing it into the environment.

Pharmaceutical compounds have been found in aquatic ecosystems since the 1990s, and Ternes,[163] Heberer,[160] and Kümmerer[164] have identified them as new uncontrolled pollutants. According to Halling-Sørensen *et al.*,[161] most pharmaceutical compounds are naturally biologically active and hydrophilic so that humans may easily absorb them, and persistent so that they do not degrade before having a healing impact. These substances of human origin are continuously released into aquatic habitats through various channels, treated wastewater being the main one. The outcome of these chemicals during wastewater treatment procedures is a key element in regulating their quantities in aquatic habitats. Antibiotics have been removed using a variety of methods, including ion exchange, coagulation,[130,165] liquid membrane separation, photo-catalytic degradation,[166] reverse osmosis, ozonation,[167] and adsorption. Adsorption is favoured over these other

Table 3 An overview of the adsorptive removal of pharmaceutical compounds by BN-based nanomaterials

BN-based nanomaterial	Pharmaceutical compounds	Initial concentration (mg L^{-1})	Maximum adsorption capacity (mg g^{-1})	Ref.
g-BN	Gatifloxacin	80	88.5	168
BN nanosheets	Tetracycline, ofloxacin & cephalexin	200	346.66, 72.50 & 225.0	172
BN	Tetracycline	10	369.79	169
BN nanosheets	Tetracycline	50 to 100	1101	170
BNNSs	Chlortetracycline hydrochloride & norfloxacin	1170 & 174	400 & 120	172
BN nanosheet	Estrone	0.05 to 12	249	173
BN bundles	Sulfadiazine & erythromycin	20 to 100	137 and 150	174
Ni–BN	Tetracycline	20 to 100	430	175
Graphene–BN aerogel	Ciprofloxacin	10.5	185	176
Carbon-doped BN	Tetracycline	40	76.7	177
BN with boron vacancies	Tetracycline	200	370	178
BNNS	Tetracycline	50 to 300	322.5	149
CoO/P-BNFs	Chlortetracycline	150	655.474	179
Carbon-modified HBN	Bisphenol-A & paracetamol	35 to 100	49.75 & 67.56	180
GO/BNF	Gemfibrozil	10.5	55.1	181
ZnTi LDH/h-BN	Amaranth & diazepam	20 & 5	99.5% & 99.8%	182
BN nanosheet	Levofloxacin	10	17.61	183
Porous hexagonal BN	Tetracycline	160	322.16	184

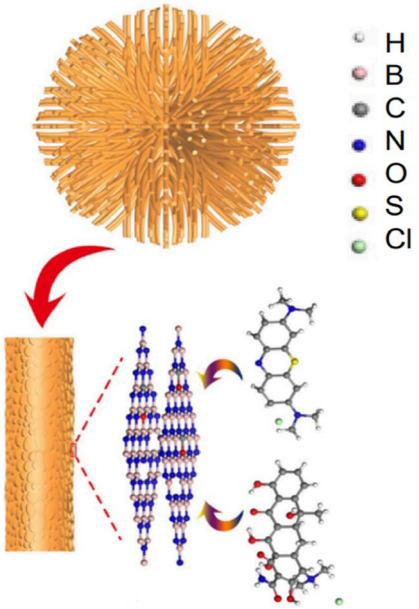

Fig. 15 Sea urchin-like hexagonal BN's potential adsorption mechanism diagram for methylene blue and tetracycline.[169]

methods because it is straightforward to design, simple to make, effective, inexpensive, and produces negligible harmful by-products. Here, we investigated the use of BN as an adsorbent in the removal of three antibiotics from water, which are tetracycline (TC), ofloxacin (OFL), and cephalexin (CFX). The summary of the adsorptive removal of pharmaceutical compounds by BN-based nanomaterials is given in Table 3.

A possible method of removing tetracycline from sea urchin-like BN adsorbents is shown in Fig. 15, which has a maximum adsorption efficiency of 370 mg g^{-1}. The structure that resembles a sea urchin was manufactured using fibres, and it has many mesopores that stretch by the centre toward the surroundings. BN adsorbents with mesoporous and large surface areas seemed particularly helpful for better adsorption. Additionally, the sea urchin-like structure also prevents the release of tetracycline. Contrary to scattered fibres and nanosheets, fibre clusters in BN nano-adsorbents with sea urchin-like forms allowed for the precipitation of organic pollutants in the core of the sea urchin, improving the adsorbing capacity. As the principal electromotive force on the BN adsorbent surface, π–π association plays a crucial role in the substantial adsorption of tetracycline with aromatic benzene ring geometries. Tetracycline physical formulations further showed Lewis basicity due to a lack of solid bonding with chlorine. As a result, interactions between sea urchin-like BN nanomaterials and Lewis acids might be the source of the removal driving force and lead to acid-base complexation.[168] Meanwhile, the introduction of carbons in BN nano-adsorbents may successfully increase the molecular orbital energy and reduce chemical stability, increasing the adsorption capability of BN nano-adsorbents that resemble sea urchins (minor stability implies better adsorption capability).[156] Moreover, the defects of the uneven BN-layered form support the improved BN adsorption performance.

Utilizing BN nanosheets containing N defects, density functional concept calculations were performed to evaluate the adsorption process for tetracycline.[170] The conventional method for chosen determining the electronic version of all linked components and interactions was the hybrid density potential with the dispersion-adjusted term, which has been successfully used in BN adsorption techniques.[171] Fig. 16 depicts the adjusted forms of pure BN nanosheets, N-defective BN nanosheets containing N vacancies, and their corresponding adsorbed forms. Complexes formed by tetracycline molecule adsorption on the nano-adsorbent surfaces were also modified. After adsorption, BN nanosheets containing N-defects have a nonplanar structure, especially in the combination of N-defective BN nanosheets containing N vacancies and tetracycline, demonstrating a strong association between them. The calculated results revealed that the association energies were −37.0 and −60.2 kcal mol^{-1} for pure BN nanosheets and tetracycline and N-defective BN nanosheets with N vacancy and tetracycline, respectively. The construction of N-defects throughout the BN nanosheet boosted the adsorptive intensities of tetracycline, enhancing the adsorption capabilities, as shown by the significantly increased interaction energy value.[170]

Tetracycline, ofloxacin, and cephalexin were used to evaluate the adsorption capability of BN nanosheets with a wide surface area to other adsorbents.[172] Graphene oxide (313 mg g^{-1}), carbon nanotubes (100 mg g^{-1}), reduced graphene oxide (35 mg g^{-1}), and activated carbon composites (262 mg g^{-1}) were all outperformed by BN nanosheets produced by advanced a 1 : 1 water/methanol mixture and a temp of 900 °C for 2 hours. The literature is quite poor in its results about ofloxacin adsorptive elimination. Activated carbon (137 mg g^{-1}), magnetite-coated zeolite (24.9 mg g^{-1}), bentonite (10.4 mg g^{-1}), and natural zeolite (16.1 mg g^{-1}) all performed less well in adsorbing cephalexin than BN nanosheets (225 mg g^{-1}). The larger surface area (1800 m^2 g^{-1}), higher pore volume (2.75 cm^3 g^{-1}), and

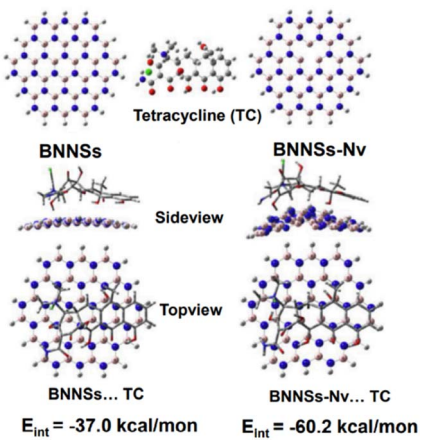

Fig. 16 Best possible structures of BN nanosheets (BNNSs) and N-defective BNNSs with N vacancy (BNNSs–Nv) and their related adsorbed forms.[170]

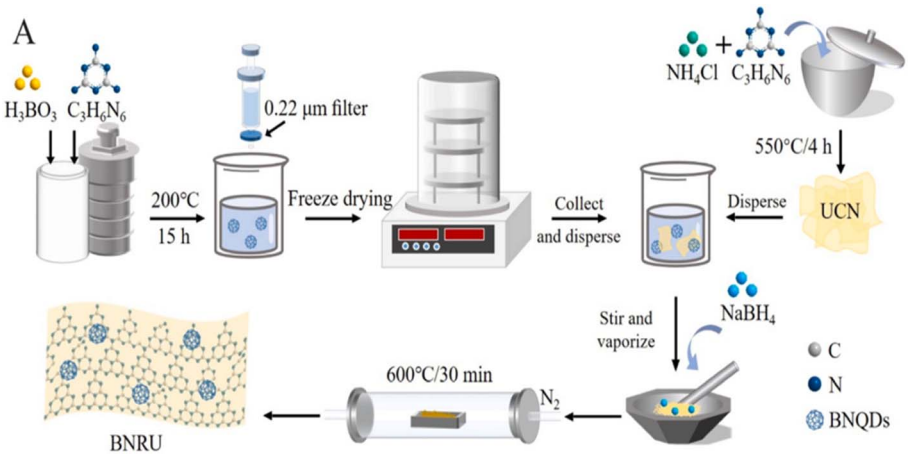

Fig. 17 Formations of BNRU.[201]

smaller sieve-like size (6.2 nm) of BN nanosheets may be responsible for their improved adsorption ability for the three antibiotics. The primary adsorption process is thought to include π–π association between the three target substances' aromatic benzene rings and the BN nanosheets' ring network.[173] In the case of tetracycline and cephalexin, a further adsorption process is connected to the amino affinity between the substances and BN nanosheets. As a result, ofloxacin had a lower adsorption capability than tetracycline and cephalexin. Tetracycline showed the highest level of adsorption among the antibiotics because it had a greater composition of aromatic benzene rings than the other antimicrobials.

4.2. Photocatalytic applications

4.2.1. Photodegradation of pharmaceuticals. Fluoroquinolone antibiotics (FQs) are often used to treat diseases in humans and animals, and this has caused ecological and environmental hazards, such as water contamination, which have received a lot of attention recently. Traditional wastewater treatment procedures are inadequate for the accurate and entire removal of FQs because of their stable chemical structure and non-biodegradable characteristics. This makes it possible for FQs to constantly reach the atmosphere through wastewater discharges. Its presence has been regularly found in various water matrices at quantities ranging from 0.6 to 5.6 μg L^{-1}.[185–187] Microbial populations and human resistance have been observed to be negatively impacted by prolonged exposure to surroundings containing FQs.[188,189] Therefore, it is critical to use eco-friendly and effective techniques to regulate and eliminate FQs from natural rivers.

The elimination of organic contaminants using semiconductor-based photocatalysis, a new wastewater treatment method, may be possible by utilizing sun energy to create active species.[190–192] Because of its high stability, cheap cost, and environmental friendliness, graphitic carbon nitride (g-C_3N_4), a metal-free semiconductor, exhibits tremendous promise for environmental remediation.[193,194] Unfortunately, the poor yields and large coupling rates of photocatalytic activity result from being concealed by visible light, insufficient oxidation abilities, and small specific surface area, and these factors continue to restrict the photocatalytic efficiency of pure g-C_3N_4 for environmental clean-up. To address the limitations of g-C_3N_4, a number of techniques have been developed, including defect engineering,[195] heterojunction design,[196] morphological controls,[197] metal/non-metal modifications,[190,198] and many others.

The h-BN can work as a co-catalyst to readily create hybrid materials with nanomaterials, and increase the number of target sites as its dimensions become closer to those of quantum dots.[199] Another benefit is that BNQDs have a lot of oxygen-containing functional groups that are negatively charged. These functional groups have a strong electrostatic attraction to photogenerated holes, which indicates that they have a lot of capability as hole channels to help separate photocarriers.[200] The merging of flow engineering and BNQDs alteration process procedures appears to be a possible way to collaboratively improve the photooxidative capabilities and carrier generation–separation performances of g-C_3N_4.

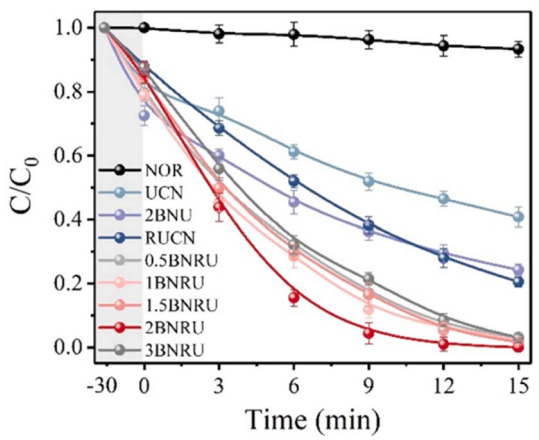

Fig. 18 NOR degradation-based photocatalytic activity.[201]

Wu *et al.*[201] developed a special BNQDs-modified reduced ultrathin g-C_3N_4 nanosheets (BNRU) metal-free photocatalyst for this investigation by combining self-assembly and thermal treatments as illustrated in Fig. 17. A visible light catalyst was employed to degrade typical FQs contaminants. Investigations into the photocatalysts' structural compositions, energy band structure, and optical and electrochemical characteristics were conducted in detail. The creation of numerous environmental factors (such as pollutant concentration, H_2O constituents, natural water matrices, solution pH, and mixed pharmaceuticals H_2O under natural solar light) was another method by which the efficiency of the BNRU technology was demonstrated. They were used to simulate actual water treatment processes.[201] Finally, feasible charge transfer methods and kinetics/pathways for pollutant degradation throughout the photocatalytic process were suggested.

NOR removal (removal of one group) studies under visible (blue-LED) light irradiation were used to assess the prepared materials' photocatalytic activity. Adsorption, direct photolysis, and photocatalysis were all shown to contribute to the elimination of NOR in Fig. 18. After 30 minutes of dark adsorption to reach adsorption–desorption equilibrium, the UCN and RUCN absorbed 20.3% and 12.2% of the NOR, respectively. With the addition of BNQDs, the NOR absorption efficiency improved, which was ascribed to chemisorption dominated by interactions between the BNQDs and NOR molecules in the form of π–π stacking interactions.[172,202] After 15 minutes of exposure to visible light, 6.7% of the NOR had been degraded without using photocatalysts, proving that a direct photolysis process was not the predominant cause of the NOR removal. The UCN only degraded 59.2% of the NOR after 15 minutes. However, the removal effectiveness increased to 79.5% when the RUCN was present. Remarkably, the BNRU composites considerably improved the effectiveness of the NOR removal, allowing ten mg L^{-1} of the NOR to decompose under the same parameters.

A pseudo-first-order kinetic model was used to determine the kinetic rate constant (K_{obs}) of the well-prepared photocatalyst for NOR degradation, as shown in Fig. 19. When BNQD packing relayed 2×10^{-2} wt%, it was evident that the BNRU composite seemed to have the maximum photocatalytic activity (2BNRU), compared to the UCN (0.0514 min^{-1}), which had a K_{obs} value of 0.3744 min^{-1}, was 7.28, 4.53, and 3.83 times higher, BNU packing with 2×10^{-2} wt% BNQDs (denoted as 2BNU), and RUCN loaded with 0.0977 min^{-1} of RUCN, proportionately. On the other hand, too many BNQDs blocked the reaction site, decreasing the photocatalytic activity.[203] As a result, 2BNRU was chosen as the best sample for future research into possible uses for the photocatalytic process.

The degradation performance against many common FQs, including ciprofloxacin (CIP), norfloxacin (NOR), ofloxacin (OFX), lomefloxacin (LOM), and enrofloxacin (ENX), was tested in order to assess the adaptability of the 2BNRU system. The removal efficiencies for ENX, CIP, LOM, OFX, and NOR, after 15 minutes of exposure utilizing the 2BNRU system, were determined to be 87.7%, 100%, 94.4%, 94.6%, and 100%, respectively, as shown in Fig. 20. According to calculations, the relevant kinetic rate constants are 0.1266, 0.3153, 0.1883, 0.188, and 0.3744, min^{-1}, as shown in Fig. 21. These results revealed that the photocatalytic method was universally applicable and

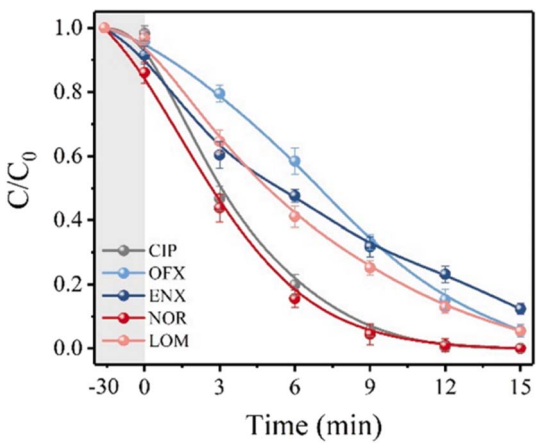

Fig. 20 Photocatalytic degradation efficiency.[201]

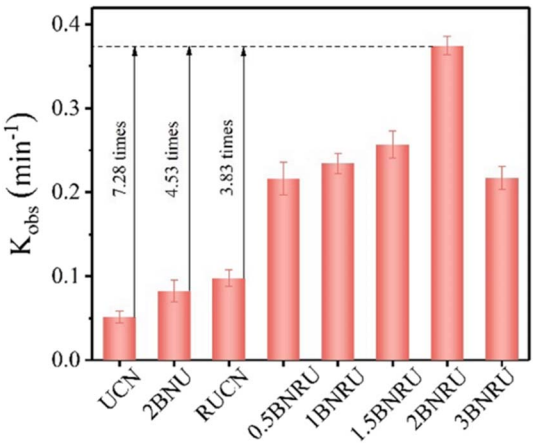

Fig. 19 Kinetic rate constant based on the photocatalytic activity.[203]

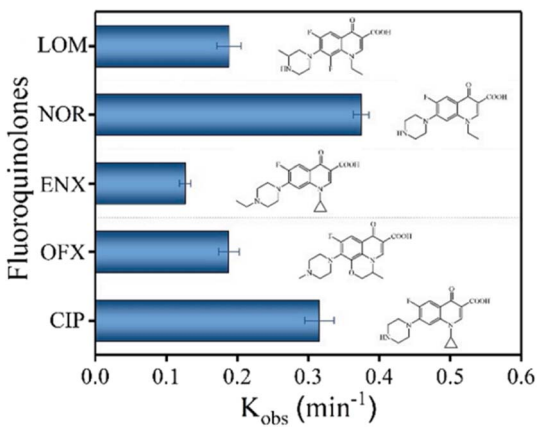

Fig. 21 Kinetic rate constants of 2BNRU for fluoroquinolones when exposed to visible light.[201]

Table 4 An overview of the photodegradation of pharmaceutical compounds by BN-based nanomaterials

BN-based nanomaterial	Pharmaceutical compounds	Initial concentration n (mg L^{-1})	Time (h)	Efficiency (%)	Ref.
g-C_3N_4 (BNRU)	Fluoroquinolone	10	0.5	46.9	201
ZnTi LDH/h-BN	Diazepam	10	2	95	182
$MnFeO_3$/h-BN	Ibuprofen	15	2	66	204
Bi_2WO_6/BN	Tetracycline & ofloxacin	20	2	99.1 & 94.66	205
Ultrathin–h-BN/Bi_2MoO_6	Tetracycline, oxytetracycline & doxycycline	20	2.33	99.19, 95.28 & 91.04	206
AuNPs/h-BN	Levofloxacin & hydrochloride	10	5	84.4	207
TiO_2–BN–Pd	Acetaminophen	1	4	90	208
BN/Fe_3O_4/MIL-53(Fe) ternary nanocomposite	Ibuprofen	10	3	100	209
BN/Bi_2MoO_6	Iohexol	20	2.5	92	210
Carbon nitride-modified boron nitride (CNBN)	Ciprofloxacin	10	4	98	211
Boron nitride/3,4,9,10-perylenetetracarboxylic dianhydride	Tetracycline	20	3	70.52	212
$SrWO_4$/BN/GCE	Ornidazole	10	3	92.4 to 99	213
$Ni(OH)_2$–TiO_2	Tetracycline	100	2	74	214
$MoSe_2$/ZnO/p-BN	Ofloxacin	30	1	99.2	215
BN/SnO_2	Salicylic acid	25	0.66	82	216
BBOB/BNQDs	Tetracycline	10	1	76.9	217
CuS/h-BN	Ibuprofen	21.20	0.5	99.2	218
Ag@CP–BNQDs	Tetracycline	10	0.5	80	219

performed better at degrading different FQs. Additionally, due to its maximum release rate, the 2BNRU photocatalytic system's degradation kinetics and processes were examined using NOR as a sample contaminant. A summary of the photocatalytic properties of the BN-based nanomaterials is given in Table 4.

4.2.2. Photodegradation of dye compounds. The colouring of materials frequently involves the use of dyes. The amounts of organic components are higher in dyes. They will seriously damage the water when they get in.[220,221] The standard dye elimination methods mainly include adsorption[222,223] and photodegradation.[224,225] Using photocatalysts to break down contaminants during light exposure, photocatalysis has been employed extensively in energy generation and environmental clean-up.[226,227]

Various photocatalytic materials only eliminate pollutants when exposed to UV light because they have broadband gaps. It has been observed that some substances, such as dyes, have the ability to sensitize a broadband gap photocatalyst by shifting their photo-excited electron into the conduction bands of the photocatalyst when exposed to visible light. This develops a photocatalyst with a broadband gap that can break down pollutants when exposed to visible light.[228,229] For instance, Gao *et al.* evaluated the photocatalytic sensitisation degradation of organic dyes when exposed to visible light.[230] By photosensitizing TiO_2 with eosin Y and rhodamine B, Diaz-Angulo *et al.* claim to have improved the photodegradation and absorption of acetaminophen and diclofenac.[231]

It has been reported that the removal of organic contaminants is significantly enhanced by the photo-deposition of platinum nanomaterials on dye-sensitized TiO_2.[232] Metal-based and metal-free photocatalysts are the two primary types of photocatalysts. Metal-based photocatalysts are used in environmental and energy-related applications (including S–TiO_2/NH_2–UiO-66,[233] and Ag/AgCl@MIL-101 (ref. 234)) because of its non-toxic and high stability.[235] The metal-free wide-bandgap photocatalyst (BN) is used due to its widespread application in water purification. Because of its extraordinarily high chemical stability, BN is widely used to eliminate contaminants from H_2O.[236] Due to its broad indirect bandgap of 5.5 eV, ultraviolet light also makes it extremely difficult to move the electron to the conduction band from the valence band in BN, so it is often not a photocatalytic material.[237] However, –OH groups are available on the surfaces of BN made using the oxygen-limiting technique. The bandgap of BN has been reported to be reduced for hydroxylation from 5.5 eV to 3.94 eV.[238]

Under UV light irradiation, BN made by this technique can break down neutral red,[239] thus implying that BN responds to UV light by acting as a photocatalytic material. We have not examined the impact of BN on how dyes break down sensitizing when subjected to visible light. Herein, the oxygen-limited technique creates BN material, and the sensitization decomposition performances of Rh-B (rhodamine B), MB (methylene blue), MO (methyl orange), Rh-B/MB and Rh-B/MO on the surface of BN under vis-light irradiation are studied.

According to Fig. 22, this removal experiment has two periods: one is adsorption, and the other is photodegradation when exposed to visible light. Using BN, Rh-B is eliminated from the water by about 87.8%, with 42.6% of that removal occurring by adsorption and the remaining 45.2% occurring *via* photodegradation. As a result of band structures, BN cannot absorb visible light and degrades Rh-B when exposed to it.[240] Under vis-light irradiation, BN was utilized to break uncoloured AT to show if it is the photocatalytic substance that responds to vis-light. BN absorbs about 10% of AT. The amount of atrazine present at the start of the photodegradation period and the conclusion of the photodegradation period is essentially the

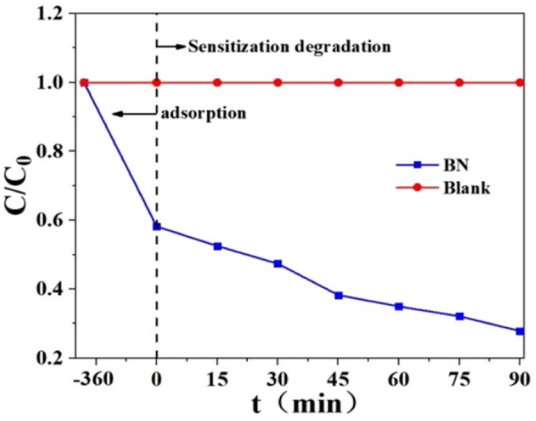

Fig. 22 Rh-B elimination by BN under vis-light irradiation.[240]

same. Because of this, BN cannot break colourless AT when exposed to visible light. Instead, Rh-B is most likely degraded by BN through a process known as sensitization photodegradation.

When exposed to vis-light, investigations are being conducted into the sensitized decomposition of methylene blue and methyl orange by BN. In accordance with Fig. 23A, 18.3% of methylene blue has been eliminated by BN under vis-light irradiation, of which 6.1% have been eliminated by adsorption, and another 12.2% have been eliminated by photodegradation.

Fig. 23B shows that 25.7% of methyl orange is eliminated, with 18.3% coming through adsorption and 7.4% coming from sensitization decomposition. The findings above demonstrate that when exposed to visible light, various dyes exhibit varying sensitization effects by BN. The greatest sensitization

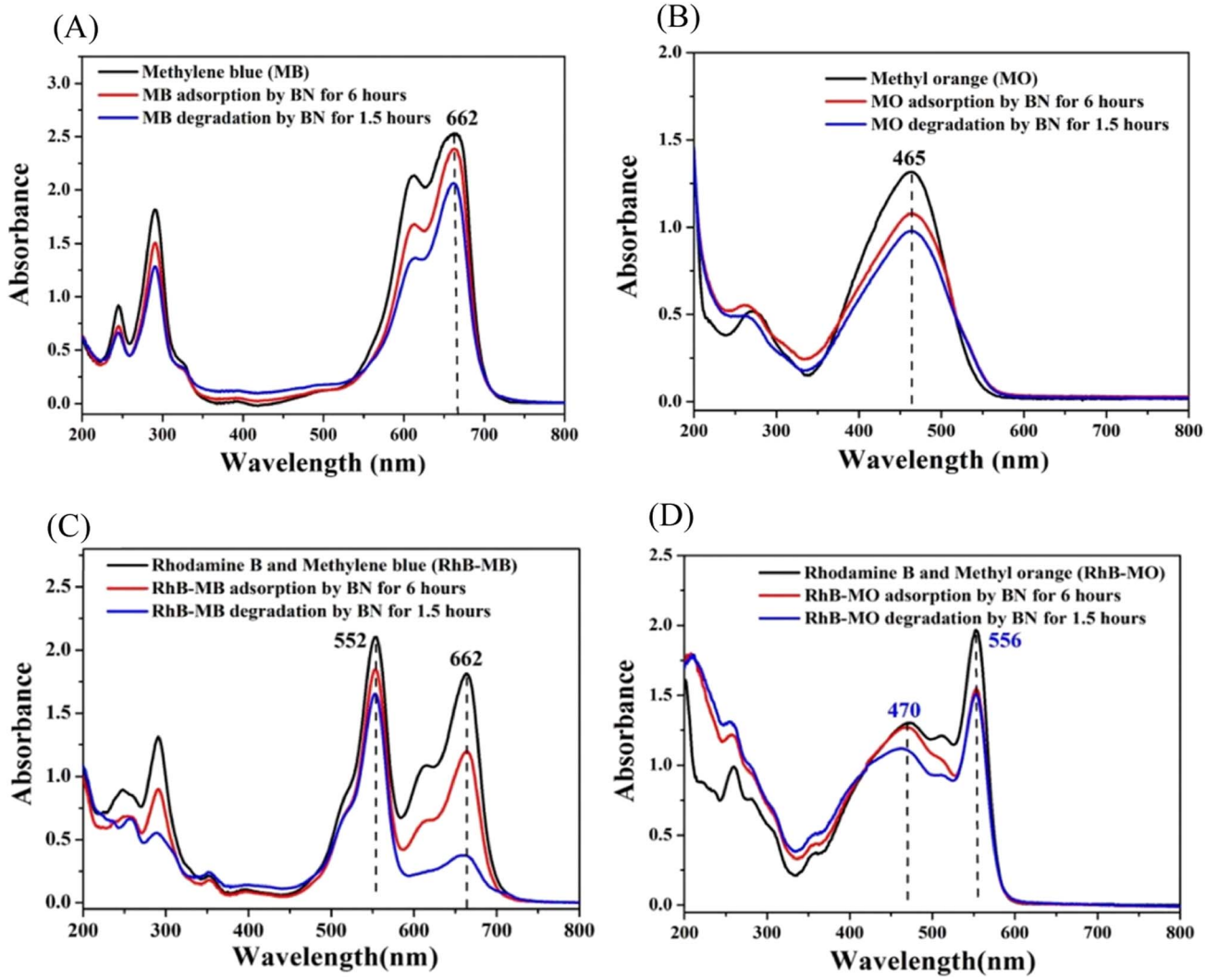

Fig. 23 (A) The ultraviolet-visible spectra of MB elimination by BN *via* adsorption and photo-removal under visible light irradiation. (B) The ultraviolet-visible spectra show the elimination of MO by BN using a combination of adsorption and photo-removal when exposed to noticeable light. (C) The Rh-B/MB solution's ultraviolet-visible spectra after being subjected to BN's adsorption and photo-removal processes while exposed to visible light. (D) The Rh-B/MO solution's UV-vis spectra after being subjected to BN's adsorption and photo-removal processes while exposed to noticeable light.[240]

photodegradation effects are produced by Rh-B (45.2%), MB (12.2%), and MO (7.4%). Rh-B is a cationic dye, and BN's surface is negatively charged (−31 mV). However, the interaction between Rh-B and BN mostly depends on hydrogen bonds (the hydrogen bond strength between the O atom in Rh-B and the H attached to the O in the BN model is 2.4 Å). Because MB has a planar structure and is also a positively charged dye, the interaction between methylene blue and BN is mostly caused *via* π–π stacking (the distance of stacking is 3.5 Å). It is vital to have a suitable e-transfer route between the BN and sensitizer so that the electron can transfer easily from the lowest unoccupied molecular orbital of a sensitizer to a conductive band of BN.[241] To let the electrons pass smoothly through the sensitizer into the photocatalytic substance, they are both frequently associated in the sensitised solar cell.[242–244] As a result, hydrogen bonds may be a richer electron transfer route than non-covalent π-interactions of aromatic rings, which explains why Rh-B's (45.2%) greater sensitization degradation efficiency than MB's (12.2%), as well as MO's (7.4%).

Researchers also looked at the sensitized degradation of the Rh-B/MB and Rh-B/MO mixture solution by BN when exposed to visible light. When Rh-B is combined with MB or MO, exciting outcomes are obtained. As shown in Fig. 23C, mixing MB and Rh-B did not produce a new UV absorption peak (662 nm for MB and 552 nm for Rh-B, respectively). This could be because Rh-B is a non-planar cation, and MB and Rh-B are both cationic dyes. As a result, in Rh-B/MB combinations, the connection between Rh-B and methylene blue is not much stronger to alter the UV absorption peaks of Rh-B and methylene blue. The ultraviolet absorption peaks of a combination of Rh-B and methylene blue are formed by superimposing their respective ultraviolet absorption peaks. The total removal of Rh-B from the Rh-B/MB combination is 21.4% (Fig. 23C), of which 12.2% is due to Rh-B's adsorption on BN, and another 9.2% is due to Rh-B's sensitization degradation on BN under visible light irradiation. A total of 79.2% of the MB in the Rh-B/MB combination (Fig. 23C) is eliminated, of which MB's adsorption on BN removes 33.8%, and another 45.4% is removed by MB's sensitization degradation on BN when exposed to visible light. This outcome is somewhat surprising, considering that Rh-B's sensitization photodegradation by BN is prohibited, and Rh-B's sensitization photodegradation by BN is promoted.

Similarly, studies are being conducted on the sensitization photodegradation of Rh-B/MO. According to Fig. 23D, the ultraviolet absorption peak of MO is responsible for the peak at 470 nm in the Rh-B/MO mixture, and the ultraviolet absorption peak of Rh-B is responsible for the peak at 556 nm in the Rh-B/MO mixture. As a result, the UV absorption peaks of Rh-B/MO are a superposition of those of Rh-B and MO. Rh-B is a positively charged dye, while methyl orange is an anion dye. They interact with each other with a greater energy of 21.2 kcal mol^{-1} than Rh-B and MB (11.5 kcal mol^{-1}). A total of 23.1% of the Rh-B in the Rh-B/MO combination is eliminated, of which 20.5% is due to Rh-B's adsorption on BN, and the remaining 2.6% is due to Rh-B's sensitization degradation on BN when exposed to visible light. In contrast, MO is eliminated from the Rh-B/MO combination by 13.9%, of which 3.2% is due to MO's adsorption on BN, and another 10.7% is due to MO's sensitization degradation on BN when exposed to visible light. As shown, the sensitisation degradation rate of Rh-B falls from 45.2% to 2.6%, while that of MO slightly increases from 7.4% to 10.7%. The summary of the photodegradation of dyes by BN-based nanomaterials is given in Table 5.

4.3. Hydrogen evolution reaction

Researchers are urged to identify alternative carbon-neutral energy vectors as part of efforts to mitigate the impact of global climate change.[259,260] In light of this, hydrogen produced from renewable sources is a prospective negligible-emission fuel and a crucial resource for the chemical sector. Because of its beneficial characteristics, like low density combined with the maximum energy densities of all substances known to man and

Table 5 An overview of the photodegradation of dyes by BN-based nanomaterials

BN-based nanomaterial	Dyes	Initial concentration n (mg L^{-1})	Efficiency (%)	Ref.
BN	Rhodamine B	20	45.2	240
BN/SnO_2	Methyl orange	25	92	216
BN–TiO_2	Rhodamine B & methylene blue	10	98 & 92	245
ZnO/BNQD-4	Methylene blue & methyl orange	10	99 & 97.9	246
BN, chitosan & graphene-based composite (BNCG)	Methylene blue	10	87	247
BN5–Ag_3/TiO_2	Methylene blue	20	98	248
BN/C_3N_4	Rhodamine B	5	97.2	249
h-BN@$PbWO_4$	Rhodamine B	5	99.9	250
$ZnFe_2O_4$/BN	Congo red	10	92	251
h-BN/Sb_2WO_6	Rhodamine B	25	80.8	252
ZnTi LDH/h-BN	Amaranth	20	100	182
BN-modified bismuth oxyiodide	Methyl orange	10	86	253
Ni–$BaTiO_3$/h-BN	Crystal violet	15	86	254
BN/Fe	Methyl orange	150	99.1	255
h-BN/NiS_2/NiS	Rhodamine B	10	98.5	256
F–BN/TiO_2	Rhodamine B	150	92	257
BN nanotubes (BNNTs)	Methyl orange	5	92	258

Table 6 Newly discovered substances with excellent photocatalytic H_2 evolution potential from water splitting in one hour time of irradiation

Photocatalyst	Catalyst loading (g)	Hydrogen evolved (μmol)	Ref.
Porous BN	0.1	12	284
B/h-BN–Ni_2P	0.05	883	274
Ni_2P/CdS	0.01	334	285
Fe_2O_3–TiO_2	0.05	880	286
MoS_2–graphene	0.15	667	287
SCu-CZS	0.01	425.5	288
Co/Cu_xS	0.01	700	289

ease of collection and transport, this finds many uses in the current environment. The potential of newly discovered nanomaterials for photocatalytic water splitting is shown in Table 6.

High manufacturing costs are one of the key obstacles to the practical use of "green" hydrogen. However, if economically reactive metal catalysts having more solar-to-hydrogen efficiency are produced, solar-driven water splitting might be a cost-effective method.[261,262] Highly active photocatalytic technologies have recently been produced employing various innovative construction techniques through 2D materials as platforms.[263–265] The h-BN is the most notable member of this family. It is excellent for various applications because of its extraordinary chemical stability and heat conductivity.[266,267] Moreover, the unfavourable oxide–metal interactions in heterogeneous catalysis can be eliminated by replacing oxide supports with h-BN.[268] This has earlier been used for things like CO_2 reduction,[269] H_2 synthesis,[270] NO_x reductions,[271] NH_3 synthesis,[272] and the oxidation of organic contaminants.[273] Recently, there has been a lot of interest in using h-BN as a catalyst-assisted material combined with different nanocomposite materials for photocatalytic activities.

Charge separation and electron transport need to be made easier by a catalyst and support that are well coupled to increase the photocatalytic activities as illustrated in Fig. 24.[274] The charge carrier separation is facilitated by the photoexcited holes being drawn to the negatively charged as-synthesized h-BN nanostructures. The adsorption of hydroxyl ions is predicted to cause a negative charge on the newly synthesized h-BN surface.[275,276] In many photocatalytic applications, the synthetic h-BN is a good catalyst support material for composite catalysts due to its inherent behaviour.[277,278] On the other hand, several methods for creating extremely effective and affordable bifunctional materials have been discovered to accelerate the hydrogen evolution process from water splitting.

Recently, NiS/Ni_2P heterostructures were synthesized by Xiao *et al.*[279] for effective electrocatalytic water splitting. Because Ni_2P has the synergistic effects of the Ni vacancy trapping electrons and the P site accepting protons, the Ni–P bond does have some charge carrier separation that is advantageous for hydrogen production.[280] The inclusion of h-BN assists in prolonging the charge carrier life period in the heterostructure, but Ni_2P itself is hampered by the quick coupling of the photogenerated charge carriers across its small band gap. The h-BN/Ni_2P

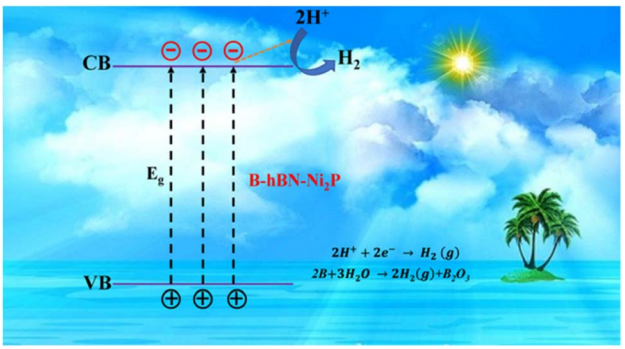

Fig. 24 Water splitting *via* photocatalytic hydrogen evolution.[274]

catalyst's band gap is adjusted for improved hydrogen formation by solar water splitting. This properly regulated band gap increased the photocatalytic activity by regulating the recoupling process of the photogenerated carriers. Additionally, it has been observed that the activity of photocatalytic hydrogen evolution may be increased by doping specific semiconductors with boron[281,282] due to B's capacity to function as a photocatalyst for the generation of hydrogen from solar water splitting, which is shown in the equation below.[283]

$$2B + 3H_2O \rightarrow 3H_2 + B_2O_3 \quad (5)$$

here, we developed an effective photocatalyst for solar water splitting *via* a simple technique of catalyst loading using surplus boron in the h-BN/Ni_2P heterostructures.

Water is photolyzed by utilizing the electrons of the electron–hole pairs produced with irradiation at low and close pH, respectively, to convert H^+ or water molecules into H_2. Photoexcited electrons move from the valence band to the conduction band of the narrow band-gap semiconductor Ni_2P when the B/h-

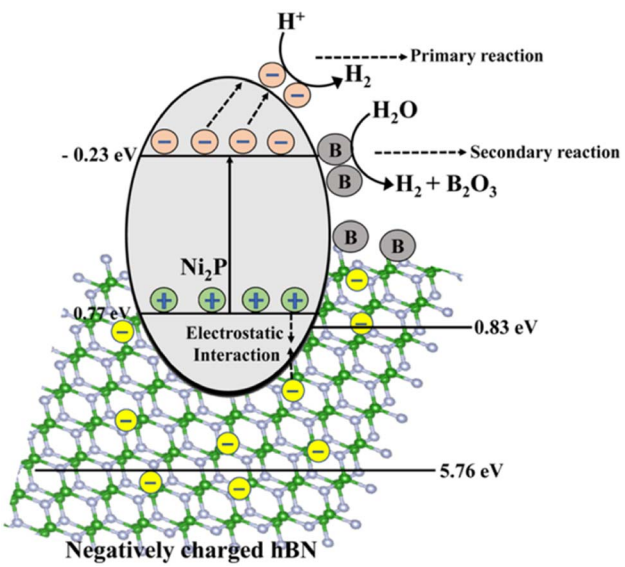

Fig. 25 The schematic illustration of the mechanism of the photocatalytic H_2 production by the B/h-BN/Ni_2P nanocomposite.[283]

BN/Ni_2P system is exposed to solar radiation, leaving holes in the valence band. The redox process, which produces hydrogen, is then started by the electrons moving toward the surface of Ni_2P's conduction band. The ionic interaction between the anionic h-BN and the holes in the valence bands of Ni_2P facilitates the further reaction. Hence, the impact of h-BN effectively boosts the activities of the photocatalyst by reducing the rate at which the charge carriers produced by photosynthesis recombine.

Similarly, in the presence of sunlight, the excess boron produced in the h-BN/Ni_2P lattice further separates water into H_2 through a secondary reaction, as seen in Fig. 25.[283] In this case, boron is not regenerated inside the photocatalytic composite and is instead oxidized to B_2O_3 under illumination together with the production of hydrogen. According to the hypothesized mechanism, Ni_2P, assisted by h-BN, acts as a major photocatalyst for hydrogen synthesis, whereas B can increase the total hydrogen production through a different reaction route.[283] Therefore, in the current system, B may be considered a "hydrogen production booster" that is depleted as the reaction progresses under irradiation. As a result, the main photocatalyst and boron work together to increase the rate at which hydrogen is produced overall. Our investigation shows that bare Ni_2P shows photocatalytic activity for producing hydrogen from splitting water.[274] Moreover, the mechanism's efficiency is increased by including h-BN, perhaps by improving the charge separation caused by photogeneration.[278] Therefore, the reactions would not completely stop even if boron were consumed. As a result, the overall impact of the catalysts improves the entire photocatalytic hydrogen-generating reaction through solar water splitting.

5. Future prospects

Although BN-based structures are becoming fantastic materials for various applications, including the removal of inorganic contaminants from water bodies and the removal of dyes and pharmaceuticals, several challenges remain.

Due to its appealing qualities, including a wide surface area, excellent chemical and mechanical strength, a lot of structural flaws, more reactive sites, and functional groups, BN-based nanomaterials exhibit confident adsorptive capability. However, numerous other study fields may need to be examined to assess the effectiveness and applicability of BN or BN-based nanomaterials more accurately.

BN-based products have little or no toxicity, according to most research studies that are currently accessible. However, it is predicted that BN nanostructures can provide environmental risks because of the complexity of nanoparticles and the unique architectures of BN particles. Compared to carbon nanotubes, some research claims that BNNTs are more cytotoxic.[290] Therefore, an in-depth investigation is required to thoroughly assess the toxicities and bio-compatibility of BN particles.

Other technological issues also present opportunities for innovation, such as creating an online tracking system for determining the purity and trace amounts of BN nanoparticles in water. Most studies on BN-based nanomaterials revealed results from laboratory tests, and the investigation is still in its early stages. Evaluating the possibilities of BN-based nanomaterials in continuous operation systems is essential. Additionally, there is enormous potential for creating brand-new, affordable, simple, profitable, and ecologically responsible processes for the high-yield preparation of BN-based products. Furthermore, it is essential to thoroughly research how BN-based products interact with contaminants. Applying analytical and characterization methods to verify the theoretically predicted adsorption mechanisms may be advantageous.

Another problem restricting the use of BN-based materials is their tendency to aggregate. The solubility of unmodified BN nanoparticles, which are often hydrophobic, in the aqueous media is another issue and a possible study topic. To develop strategies for simple dispersions, study of the surfaces of these materials must be carried out, as must research on synthetic methods. Although numerous types of research have documented the synthesis and characterization of BN materials, further research is required to broaden this research area. It is

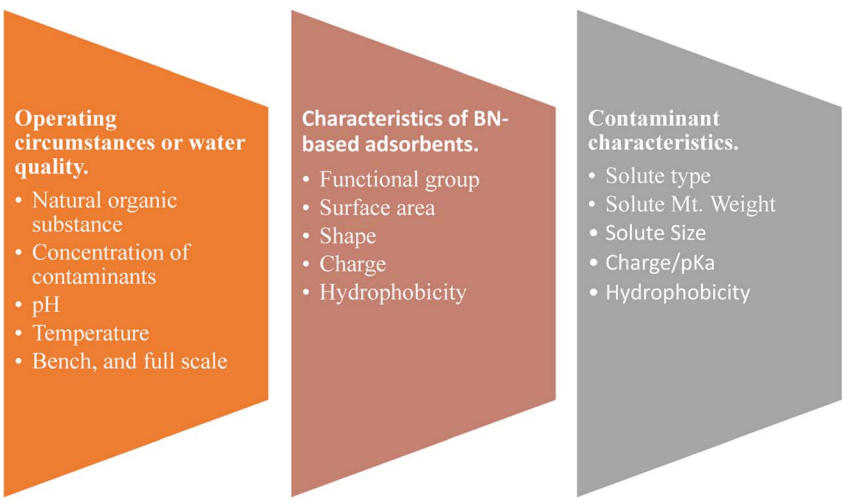

Fig. 26 Future research areas for BN-based nanoparticles used as adsorbents.

necessary to investigate suitable operationalized techniques and materials to produce BN materials with the requisite characteristics for particular applications. The solubility and the dispersibility of BN nanoparticles in water may be enhanced *via* chemical functionalization.[291]

Like most new materials, BN-based compounds have not been used in actual applications to address genuine water purification issues. Researchers need to examine whether it is possible to use these incredible materials in practical applications. This necessitates the creation of a system that can produce BN-based products in large quantities at a reasonable cost, as well as evaluating many commercial and economic factors. BN-based compounds have not been evaluated in many sections of the water purification industry. For instance, the desalination capabilities of these materials have not received much attention. Researchers might focus on using these materials in various desalination systems to assess their effectiveness.

Using BN materials with antibacterial properties might create new possibilities for post- or pre-treatment water and desalination. Numerous theoretical studies have also predicted the exceptional qualities of BN materials in purifying water. Researchers must concentrate on creating novel BN structures and consider alternative environmental uses for old and new BN materials. There is a high probability that BN-based materials will soon be introduced to the market. Based on recent positive results, it may be reasonably predicted that BN-based materials may become the future water purification materials. Fig. 26 summarises the potential main areas of future research on BN-based nanomaterials from the perspective of pollutant qualities, wastewater quality conditions, and BN-based adsorbent capabilities.

6. Conclusion

Currently, BN is the most encouraging nanomaterial. This paper describes various applications of BN, which was earlier considered a synthetic material of no advantageous use. In a broad spectrum of introspection, it is widely used in heavy metals, dyes, and pharmaceutical adsorption. Basic methods to synthesise nanomaterials include mechanical exfoliation, chemical exfoliation, and chemical vapour deposition. It also avails a greener synthesis method, *i.e.*, green dry ice-assisted ball milling. The fundamental properties that it holds enhance its beauty in the field of its application, like large surface area, mechanical stiffness, thermal stability, and superior thermal conductivity for which it is attractive for the adsorption of various inorganic (heavy metals) and organic pollutants, mainly dyes and antibiotics, and the information they give can be useful for the treatment of water and wastewater. Its uses in photodegradation are highly appreciated and engulfed to remove organic pollutants. Hydrogen evolution from water splitting is also carried out because of its low density, combined with the highest energy densities of all substances known to man and ease of storage and transportation.

Conflicts of interest

There are no conflicts to declare.

References

1 L. F. Dobrzhinetskaya, R. Wirth, J. Yang, H. W. Green, I. D. Hutcheon, P. K. Weber and E. S. Grew, *Am. Mineral.*, 2014, **99**, 764–772.
2 Y. Shimizu, Y. Moriyoshi, H. Tanaka and S. Komatsu, *Appl. Phys. Lett.*, 1999, **75**, 929.
3 D. Golberg, Y. Bando, O. Stéphan and K. Kurashima, *Appl. Phys. Lett.*, 1998, **73**, 2441–2443.
4 C. Tang, Y. Bando and D. Golberg, *Chem. Commun.*, 2002, **2**, 2826–2827.
5 Y. Saito, M. Maida and T. Matsumoto, *Jpn. J. Appl. Phys., Part 1*, 1999, **38**, 159–163.
6 Z. G. Chen, J. Zou, G. Liu, F. Li, Y. Wang, L. Wang, X. L. Yuan, T. Sekiguchi, H. M. Cheng and G. Q. Lu, *ACS Nano*, 2008, **2**, 2183–2191.
7 Y. Qiu, J. Yu, J. Yin, C. Tan, X. Zhou, X. Bai and E. Wang, *Nanotechnology*, 2009, **20**, 345603.
8 H. Zhang, J. Yu, Y. Chen and J. F. Gerald, *J. Am. Ceram. Soc.*, 2006, **89**, 675–679.
9 R. Haubner, M. Wilhelm, R. Weissenbacher and B. Lux, *High Performance Non-Oxide Ceramics II*, 2002, vol. 102, pp. 1–45.
10 M. Corso, W. Auwärter, M. Muntwiler, A. Tamai, T. Greber and J. Osterwalder, *Science*, 2004, **303**, 217–220.
11 D. Golberg, Y. Bando, Y. Huang, T. Terao, M. Mitome, C. Tang and C. Zhi, *ACS Nano*, 2010, **4**, 2979–2993.
12 Y. Lin, T. V. Williams and J. W. Connell, *J. Phys. Chem. Lett.*, 2010, **1**, 277–283.
13 P. Ma and J. T. Spencer, *J. Mater. Sci.*, 2015, **50**, 313–323.
14 L. Ci, L. Song, C. Jin, D. Jariwala, D. Wu, Y. Li, A. Srivastava, Z. F. Wang, K. Storr, L. Balicas, F. Liu and P. M. Ajayan, *Nat. Mater.*, 2010, **9**, 430–435.
15 G. Elumalai, H. Noguchi and K. Uosaki, *Phys. Chem. Chem. Phys.*, 2014, **16**, 13755–13761.
16 H. B. Cho, Y. Tokoi, S. Tanaka, H. Suematsu, T. Suzuki, W. Jiang, K. Niihara and T. Nakayama, *Compos. Sci. Technol.*, 2011, **71**, 1046–1052.
17 X. Wang, A. Pakdel, J. Zhang, Q. Weng, T. Zhai, C. Zhi, D. Golberg and Y. Bando, *Nanoscale Res. Lett.*, 2012, **7**, 1–7.
18 W.-L. Song, P. Wang, L. Cao, A. Anderson, M. J. Meziani, A. J. Farr and Y.-P. Sun, *Angew. Chem.*, 2012, **124**, 6604–6607.
19 J. Yu, X. Huang, C. Wu, X. Wu, G. Wang and P. Jiang, *Polymer*, 2012, **53**, 471–480.
20 K. Watanabe, T. Taniguchi and H. Kanda, *Nat. Mater.*, 2004, **3**, 404–409.
21 C. R. Dean, A. F. Young, I. Meric, C. Lee, L. Wang, S. Sorgenfrei, K. Watanabe, T. Taniguchi, P. Kim, K. L. Shepard and J. Hone, *Nat. Nanotechnol.*, 2010, **5**, 722–726.
22 Z. Q. Duan, Y. T. Liu, X. M. Xie and X. Y. Ye, *Chin. Chem. Lett.*, 2013, **24**, 17–19.
23 M. Emanet, Ö. Şen, Z. Çobandede and M. Çulha, *Colloids Surf., B*, 2015, **134**, 440–446.
24 R. Agrawal, A. Nieto, H. Chen, M. Mora and A. Agarwal, *ACS Appl. Mater. Interfaces*, 2013, **5**, 12052–12057.
25 Z. Zheng, M. C. Cox and B. Li, *J. Mater. Sci.*, 2017, **53**, 66–99.

26 Y. L. Zhou, J. F. Zhi, P. F. Wang, Y. M. Chong, Y. S. Zou, W. J. Zhang and S. T. Lee, *Appl. Phys. Lett.*, 2008, **92**, 163105.
27 V. Raffa, G. Ciofani and A. Cuschieri, *Nanotechnology*, 2009, **20**, 075104.
28 Q. Weng, B. Wang, X. Wang, N. Hanagata, X. Li, D. Liu, X. Wang, X. Jiang, Y. Bando and D. Golberg, *ACS Nano*, 2014, **8**, 6123–6130.
29 C. Zhi, Y. Bando, T. Terao, C. Tang, H. Kuwahara and D. Golberg, *Adv. Funct. Mater.*, 2009, **19**, 1857–1862.
30 X. Huang, C. Zhi, P. Jiang, D. Golberg, Y. Bando and T. Tanaka, *Adv. Funct. Mater.*, 2013, **23**, 1824–1831.
31 C. Zhi, Y. Bando, C. Tang, H. Kuwahara and D. Golberg, *Adv. Mater.*, 2009, **21**, 2889–2893.
32 T. Guo, P. Nikolaev, A. G. Rinzler, D. Tomanek, D. T. Colbert and R. E. Smalley, *J. Phys. Chem.*, 1995, **99**, 10694–10697.
33 S. Dai, Z. Fei, Q. Ma, A. S. Rodin, M. Wagner, A. S. McLeod, M. K. Liu, W. Gannett, W. Regan, K. Watanabe, T. Taniguchi, M. Thiemens, G. Dominguez, A. H. Castro Neto, A. Zettl, F. Keilmann, P. Jarillo-Herrero, M. M. Fogler and D. N. Basov, *Science*, 2014, **343**, 1125–1129.
34 J. D. Caldwell, A. V. Kretinin, Y. Chen, V. Giannini, M. M. Fogler, Y. Francescato, C. T. Ellis, J. G. Tischler, C. R. Woods, A. J. Giles, M. Hong, K. Watanabe, T. Taniguchi, S. A. Maier and K. S. Novoselov, *Nat. Commun.*, 2014, **5**, 1–9.
35 A. Woessner, M. B. Lundeberg, Y. Gao, A. Principi, P. Alonso-González, M. Carrega, K. Watanabe, T. Taniguchi, G. Vignale, M. Polini, J. Hone, R. Hillenbrand and F. H. L. Koppens, *Nat. Mater.*, 2014, **14**, 421–425.
36 S. Dai, Q. Ma, M. K. Liu, T. Andersen, Z. Fei, M. D. Goldflam, M. Wagner, K. Watanabe, T. Taniguchi, M. Thiemens, F. Keilmann, G. C. A. M. Janssen, S. E. Zhu, P. Jarillo-Herrero, M. M. Fogler and D. N. Basov, *Nat. Nanotechnol.*, 2015, **10**, 682–686.
37 T. T. Tran, K. Bray, M. J. Ford, M. Toth and I. Aharonovich, *Nat. Nanotechnol.*, 2015, **11**, 37–41.
38 A. J. Giles, S. Dai, I. Vurgaftman, T. Hoffman, S. Liu, L. Lindsay, C. T. Ellis, N. Assefa, I. Chatzakis, T. L. Reinecke, J. G. Tischler, M. M. Fogler, J. H. Edgar, D. N. Basov and J. D. Caldwell, *Nat. Mater.*, 2017, **17**, 134–139.
39 T. Q. P. Vuong, S. Liu, A. Van Der Lee, R. Cuscó, L. Artús, T. Michel, P. Valvin, J. H. Edgar, G. Cassabois and B. Gil, *Nat. Mater.*, 2017, **17**, 152–158.
40 T. Taniguchi and K. Watanabe, *J. Cryst. Growth*, 2007, **303**, 525–529.
41 X. Z. Du, J. Li, J. Y. Lin and H. X. Jiang, *Appl. Phys. Lett.*, 2016, **108**, 052106.
42 Y. J. Cho, A. Summerfield, A. Davies, T. S. Cheng, E. F. Smith, C. J. Mellor, A. N. Khlobystov, C. T. Foxon, L. Eaves, P. H. Beton and S. V. Novikov, *Sci. Rep.*, 2016, **6**, 1–7.
43 T. Q. P. Vuong, G. Cassabois, P. Valvin, E. Rousseau, A. Summerfield, C. J. Mellor, Y. Cho, T. S. Cheng, J. D. Albar, L. Eaves, C. T. Foxon, P. H. Beton, S. V. Novikov and B. Gil, *2D Mater.*, 2017, **4**, 021023.
44 J. D. Caldwell, I. Aharonovich, G. Cassabois, J. H. Edgar, B. Gil and D. N. Basov, *Nat. Rev. Mater.*, 2019, **4**, 552–567.
45 J. Koskelo, G. Fugallo, M. Hakala, M. Gatti, F. Sottile and P. Cudazzo, *Phys. Rev. B*, 2017, **95**, 035125.
46 E. Yoxall, M. Schnell, A. Y. Nikitin, O. Txoperena, A. Woessner, M. B. Lundeberg, F. Casanova, L. E. Hueso, F. H. L. Koppens and R. Hillenbrand, *Nat. Photonics*, 2015, **9**, 674–678.
47 O. Hassel, *BN. Norsk. Geol. Tidskr.*, 1926, **9**, 266.
48 A. Brager, *Acta Physicochim. URSS*, 1937, **7**, 699–706.
49 E. A. Wood and IUCr, *Acta Crystallogr.*, 1951, **4**, 353–362.
50 J. Tersoff, *Phys. Rev. B: Condens. Matter Mater. Phys.*, 1988, **38**, 9902.
51 S. Plimpton, *J. Comput. Phys.*, 1995, **117**, 1–19.
52 A. Stukowski, *Modell. Simul. Mater. Sci. Eng.*, 2009, **18**, 015012.
53 W. Humphrey, A. Dalke and K. Schulten, *J. Mol. Graphics*, 1996, **14**, 33–38.
54 V. D. Blank, D. V. Batov, B. A. Kulnitskiy, E. V. Polyakov, I. A. Perezhogin, D. A. Podgorny and Y. N. Parkhomenko, *Journal of Superhard Materials*, 2007, **29**, 206–212.
55 P. M. Ajayan and T. W. Ebbesen, *Rep. Prog. Phys.*, 1997, **60**, 1025.
56 Y. S. Buranova, B. A. Kulnitskiy, I. A. Perezhogin and V. D. Blank, *Crystallogr. Rep.*, 2015, **60**, 90–94.
57 D. Golberg, Y. Bando, K. Kurashima and T. Sato, *Solid State Commun.*, 2000, **116**, 1–6.
58 R. Ma and Y. Bando, *Sci. Technol. Adv. Mater.*, 2003, **4**, 403–407.
59 L. Y. Heng, A. Chou, J. Yu, Y. Chen and J. J. Gooding, *Electrochem. Commun.*, 2005, **7**, 1457–1462.
60 R. Ma, Y. Bando, T. Sato, D. Golberg, H. Zhu, C. Xu and D. Wu, *Appl. Phys. Lett.*, 2002, **81**, 5225.
61 T. Oku, K. Hiraga, T. Matsuda, T. Hirai and M. Hirabayashi, *Diamond Relat. Mater.*, 2003, **12**, 1138–1145.
62 K. S. Novoselov, D. Jiang, F. Schedin, T. J. Booth, V. V. Khotkevich, S. V. Morozov and A. K. Geim, *Proc. Natl. Acad. Sci. U. S. A.*, 2005, **102**, 10451–10453.
63 J. C. Meyer, A. Chuvilin, G. Algara-Siller, J. Biskupek and U. Kaiser, *Nano Lett.*, 2009, **9**, 2683–2689.
64 R. V. Gorbachev, I. Riaz, R. R. Nair, R. Jalil, L. Britnell, B. D. Belle, E. W. Hill, K. S. Novoselov, K. Watanabe, T. Taniguchi, A. K. Geim and P. Blake, *Small*, 2011, **7**, 465–468.
65 L. H. Li, Y. Chen, G. Behan, H. Zhang, M. Petravic and A. M. Glushenkov, *J. Mater. Chem.*, 2011, **21**, 11862–11866.
66 J. N. Coleman, M. Lotya, A. O'Neill, S. D. Bergin, P. J. King, U. Khan, K. Young, A. Gaucher, S. De, R. J. Smith, I. V. Shvets, S. K. Arora, G. Stanton, H. Y. Kim, K. Lee, G. T. Kim, G. S. Duesberg, T. Hallam, J. J. Boland, J. J. Wang, J. F. Donegan, J. C. Grunlan, G. Moriarty, A. Shmeliov, R. J. Nicholls, J. M. Perkins, E. M. Grieveson, K. Theuwissen, D. W. McComb, P. D. Nellist and V. Nicolosi, *Science*, 2011, **331**, 568–571.

67 O. R. Lourie, C. R. Jones, B. M. Bartlett, P. C. Gibbons, R. S. Ruoff and W. E. Buhro, *Chem. Mater.*, 2000, **12**, 1808–1810.
68 W. Auwärter, H. U. Suter, H. Sachdev and T. Greber, *Chem. Mater.*, 2004, **16**, 343–345.
69 F. Müller, K. Stöwe and H. Sachdev, *Chem. Mater.*, 2005, **17**, 3464–3467.
70 X. Song, J. Gao, Y. Nie, T. Gao, J. Sun, D. Ma, Q. Li, Y. Chen, C. Jin, A. Bachmatiuk, M. H. Rümmeli, F. Ding, Y. Zhang and Z. Liu, *Nano Res.*, 2015, **8**, 3164–3176.
71 P. Ahmad, M. U. Khandaker, Y. M. Amin and Z. R. Khan, *AIP Conf. Proc.*, 2015, **1657**, 100010.
72 R. Arenal, O. Stephan, J. Lou Cochon and A. Loiseau, *J. Am. Chem. Soc.*, 2007, **129**, 16183–16189.
73 D. Golberg, Y. Bando, M. Eremets, K. Takemura, K. Kurashima and H. Yusa, *Appl. Phys. Lett.*, 1998, **69**, 2045.
74 D. P. Yu, X. S. Sun, C. S. Lee, I. Bello, S. T. Lee, H. D. Gu, K. M. Leung, G. W. Zhou, Z. F. Dong and Z. Zhang, *Appl. Phys. Lett.*, 1998, **72**, 1966.
75 O. Stephan, P. M. Ajayan, C. Colliex, P. Redlich, J. M. Lambert, P. Bernier and P. Lefin, *Science*, 1994, **266**, 1683–1685.
76 J. Cumings and A. Zettl, *Chem. Phys. Lett.*, 2000, **316**, 211–216.
77 C. Y. Zhang, X. L. Zhong, J. B. Wang and G. W. Yang, *Chem. Phys. Lett.*, 2003, **370**, 522–527.
78 W. Q. Han, H. G. Yu and Z. Liu, *Appl. Phys. Lett.*, 2011, **98**, 203112.
79 W. Han, Y. Bando, K. Kurashima and T. Sato, *Appl. Phys. Lett.*, 1998, **73**, 3085.
80 R. Gao, L. Yin, C. Wang, Y. Qi, N. Lun, L. Zhang, Y. X. Liu, L. Kang and X. Wang, *J. Phys. Chem. C*, 2009, **113**, 15160–15165.
81 B. T. Branson, P. S. Beauchamp, J. C. Beam, C. M. Lukehart and J. L. Davidson, *ACS Nano*, 2013, **7**, 3183–3189.
82 M. Hemmat Esfe, A. Naderi, M. Akbari, M. Afrand and A. Karimipour, *J. Therm. Anal. Calorim.*, 2015, **121**, 1273–1278.
83 H. Zhao, J. Ding, B. Xu, X. Zhao, Y. Zheng, Z. Shao and H. Yu, *ACS Sustain. Chem. Eng.*, 2019, **7**, 14266–14272.
84 A. Lipp, K. A. Schwetz and K. Hunold, *J. Eur. Ceram. Soc.*, 1989, **5**, 3–9.
85 V. Vatanpour, S. A. Naziri Mehrabani, B. Keskin, N. Arabi, B. Zeytuncu and I. Koyuncu, *Ind. Eng. Chem. Res.*, 2021, **60**, 13391–13424.
86 C. Zhou, C. Lai, C. Zhang, G. Zeng, D. Huang, M. Cheng, L. Hu, W. Xiong, M. Chen, J. Wang, Y. Yang and L. Jiang, *Appl. Catal., B*, 2018, **238**, 6–18.
87 Y. G. Park, S. N. Nam, M. Jang, C. Min Park, N. Her, J. Sohn, J. Cho and Y. Yoon, *Sep. Purif. Technol.*, 2022, **288**, 120637.
88 R. Arora, *Mater. Today: Proc.*, 2019, **18**, 4745–4750.
89 T. Meng, C. Wang, W. J. Florkowski and Z. Yang, *Aquac. Econ. Manag.*, 2023, **27**, 1–24, DOI: **10.1080/13657305.2021.1996480**.
90 M. K. Sharma, C. K. Jain, V. K. Choubey and D. C. Singhal, *Environ. Monit. Assess.*, 2008, **157**, 11–21.
91 F. Han, Y. Zong, D. Jassby, J. Wang and J. Tian, *Environ. Res.*, 2020, **183**, 109240.
92 Q. Zhu and Z. Li, *Chem. Eng. J.*, 2015, **281**, 69–80.
93 Y. Xie, X. Yuan, Z. Wu, G. Zeng, L. Jiang, X. Peng and H. Li, *J. Colloid Interface Sci.*, 2019, **536**, 440–455.
94 X. Zhao, Y. Wang, H. Wu, L. Fang, J. Liang, Q. Fan and P. Li, *J. Mol. Liq.*, 2017, **248**, 1030–1038.
95 J. Li, X. Xiao, X. Xu, J. Lin, Y. Huang, Y. Xue, P. Jin, J. Zou and C. Tang, *Sci. Rep.*, 2013, **3**, 1–7.
96 R. S. Bangari, V. K. Yadav, J. K. Singh and N. Sinha, *ACS Omega*, 2020, **5**, 10301–10314.
97 W. Shen, Q. Guo, Y. Zhang, Y. Liu, J. Zheng, J. Cheng and J. Fan, *Colloids Surf., A*, 2006, **273**, 147–153.
98 W. Da Oh, M. G. H. Lee, W. D. Chanaka Udayanga, A. Veksha, Y. Bao, A. Giannis, J. W. Lim and G. Lisak, *J. Environ. Chem. Eng.*, 2019, **7**, 102872.
99 J. Li, P. Jin, W. Dai, C. Wang, R. Li, T. Wu and C. Tang, *Mater. Chem. Phys.*, 2017, **196**, 186–193.
100 T. Liu, Y. L. Li, J. Y. He, Y. Hu, C. M. Wang, K. S. Zhang, X. J. Huang, L. T. Kong and J. H. Liu, *New J. Chem.*, 2019, **43**, 3280–3290.
101 M. Wang, Y. Bai, B. Zhang, B. Zhong, Y. Yu, J. Zhang, X. Huang and G. Wen, *Ceram. Int.*, 2019, **45**, 6684–6692.
102 R. S. Bangari, A. K. Singh, S. Namsani, J. K. Singh and N. Sinha, *ACS Appl. Mater. Interfaces*, 2019, **11**, 19017–19028.
103 P. Karthikeyan, S. S. D. Elanchezhiyan, J. Preethi, S. Meenakshi and C. M. Park, *Appl. Surf. Sci.*, 2020, **511**, 145543.
104 S. Wang, G. Wang, T. Wu, Y. Zhang, F. Zhan, Y. Wang, J. Wang, Y. Fu and J. Qiu, *J. Mater. Chem. A*, 2018, **6**, 14644–14650.
105 Z. Song, K. Guo, W. Bai and C. Tang, *J. Solid State Chem.*, 2023, **317**, 123720.
106 P. Zhang, Y. Chen, Q. Guo, Y. Liu, H. Chong, H. Weng, X. Zhao, Y. Yang and M. Lin, *Sep. Purif. Technol.*, 2023, **305**, 122538.
107 X. Gao, X. Huang, J. Lin, C. Yu, C. Tang and Y. Huang, *Soft Matter*, 2023, **19**, 973–982.
108 U. Lawal Usman, B. Kumar Allam, N. Bahadur Singh and S. Banerjee, *J. Mol. Liq.*, 2022, **354**, 118833.
109 J. Kou, X. Wei, H. Wu, W. Linghu, G. Sheng and Y. Pan, *J. Mol. Liq.*, 2022, **359**, 119355.
110 Y. Chen, P. Zhang, L. Jiao, G. Chen, Y. Yang, H. Chong and M. Lin, *Chem. Eng. J.*, 2022, **446**, 137337.
111 S. Li, F. Liu, Y. Su, N. Shao, D. Yu, Y. Liu, W. Liu and Z. Zhang, *J. Hazard. Mater.*, 2019, **378**, 120669.
112 L. Li, K. Chang, P. Fang, K. Du, C. Chen, S. Zhou, C. Shen, W. Linghu, G. Sheng, T. Hayat and X. Guo, *Appl. Surf. Sci.*, 2020, **521**, 146373.
113 T. Liu, Y. Li, J. He, K. Zhang, Y. Hu, X. Chen, C. Wang, X. Huang, L. Kong and J. Liu, *J. Mater. Sci.*, 2019, **54**, 5366–5380.
114 L. L. Ling, W. J. Liu, S. Zhang and H. Jiang, *Environ. Sci. Technol.*, 2017, **51**, 10081–10089.

115 F. khan, N. Abdul, I. U. Din, T. Saeed, M. A. Alotaibi, A. I. Alharthi, A. Habib and T. Malik, *Ceram. Int.*, 2021, **47**, 4749–4757.
116 D. Peng, W. Jiang, F. F. Li, L. Zhang, R. P. Liang and J. D. Qiu, *ACS Sustain. Chem. Eng.*, 2018, **6**, 11685–11694.
117 Y. Zhang, G. Wang, S. Wang, J. Wang and J. Qiu, *J. Colloid Interface Sci.*, 2019, **552**, 604–612.
118 G. Yadav, S. R. Mishra, V. Gadore, N. Yadav and M. Ahmaruzzaman, *Sci. Rep.*, 2023, **13**, 1–21.
119 A. K. Dey, S. R. Mishra and M. Ahmaruzzaman, *Environ. Sci. Pollut. Res.*, 2023, **30**, 53887–53903.
120 Y. Wang, Y. Mu, Q. B. Zhao and H. Q. Yu, *Sep. Purif. Technol.*, 2006, **50**, 1–7.
121 H. Liu, P. Li, T. Zhang, Y. Zhu and F. Qiu, *Food Bioprod. Process.*, 2020, **119**, 257–267.
122 V. Gadore, S. R. Mishra and M. Ahmaruzzaman, *Sci. Rep.*, 2023, **13**, 7708.
123 S. Nethaji and A. Sivasamy, *Chemosphere*, 2011, **82**, 1367–1372.
124 J. Wang, T. Tsuzuki, B. Tang, X. Hou, L. Sun and X. Wang, *ACS Appl. Mater. Interfaces*, 2012, **4**, 3084–3090.
125 M. Ghaedi, M. Ghayedi, S. N. Kokhdan, R. Sahraei and A. Daneshfar, *J. Ind. Eng. Chem.*, 2013, **19**, 1209–1217.
126 A. Mirzaei, A. Ebadi and P. Khajavi, *Chem. Eng. J.*, 2013, **231**, 550–560.
127 L. Malaeb and G. M. Ayoub, *Desalination*, 2011, **267**, 1–8.
128 F. Han, V. S. R. Kambala, M. Srinivasan, D. Rajarathnam and R. Naidu, *Appl. Catal., A*, 2009, **359**, 25–40.
129 A. Lee, J. W. Elam and S. B. Darling, *Environ. Sci.: Water Res. Technol.*, 2016, **2**, 17–42.
130 C. Sheng, A. G. A. Nnanna, Y. Liu and J. D. Vargo, *Sci. Total Environ.*, 2016, **550**, 1075–1083.
131 M. Ptaszkowska-Koniarz, J. Goscianska and R. Pietrzak, *J. Colloid Interface Sci.*, 2017, **504**, 549–560.
132 Y. D. Liang, Y. J. He, T. T. Wang and L. H. Lei, *Journal of Water Process Engineering*, 2019, **27**, 77–88.
133 R. S. Bangari, A. Yadav and N. Sinha, *Soft Matter*, 2021, **17**, 2640–2651.
134 J. Li, Y. Huang, Z. Liu, J. Zhang, X. Liu, H. Luo, Y. Ma, X. Xu, Y. Lu, J. Lin, J. Zou and C. Tang, *J. Mater. Chem. A*, 2015, **3**, 8185–8193.
135 Z. Zhou, J. Zhao, Z. Chen, X. Gao, T. Yan, B. Wen and P. Von Ragué Schleyer, *J. Phys. Chem. B*, 2006, **110**, 13363–13369.
136 M. X. Zhu, L. Lee, H. H. Wang and Z. Wang, *J. Hazard. Mater.*, 2007, **149**, 735–741.
137 Y. Guo, R. Wang, P. Wang, L. Rao and C. Wang, *ACS Sustain. Chem. Eng.*, 2019, **7**, 5727–5741.
138 P. Wang, C. Wu, Y. Guo and C. Wang, *Phys. Chem. Chem. Phys.*, 2016, **18**, 30196–30203.
139 P. Wang, Y. Yin, Y. Guo and C. Wang, *RSC Adv.*, 2016, **6**, 10615–10624.
140 Y. Yan, M. Zhang, K. Gong, L. Su, Z. Guo and L. Mao, *Chem. Mater.*, 2005, **17**, 3457–3463.
141 J. Fu, Z. Chen, M. Wang, S. Liu, J. Zhang, J. Zhang, R. Han and Q. Xu, *Chem. Eng. J.*, 2015, **259**, 53–61.
142 Y. Li, Q. Du, T. Liu, J. Sun, Y. Wang, S. Wu, Z. Wang, Y. Xia and L. Xia, *Carbohydr. Polym.*, 2013, **95**, 501–507.
143 T. Shen, S. Liu, W. Yan and J. Wang, *J. Mater. Sci.*, 2019, **54**, 8852–8859.
144 Q. Li, T. Yang, Q. Yang, F. Wang, K. C. Chou and X. Hou, *Ceram. Int.*, 2016, **42**, 8754–8762.
145 J. Pang, Y. Chao, H. Chang, H. Li, J. Xiong, Q. Zhang, G. Chen, J. Qian, W. Zhu and H. Li, *ACS Sustain. Chem. Eng.*, 2018, **6**, 4948–4957.
146 V. Ugraskan, B. Isik and O. Yazici, *Chem. Eng. Commun.*, 2022, **209**, 1111–1129.
147 A. S. Krishna Kumar, J. Warchol, J. Matusik, W. L. Tseng, N. Rajesh and T. Bajda, *npj Clean Water*, 2022, **5**, 1–12.
148 R. S. Bangari, A. Yadav, J. Bharadwaj and N. Sinha, *J. Environ. Chem. Eng.*, 2022, **10**, 107052.
149 R. S. Bangari, A. Yadav, P. Awasthi and N. Sinha, *Colloids Surf., A*, 2022, **634**, 127943.
150 C. Xu, J. Zeng, X. Gu, Y. Wang, E. Li, C. Zhang, C. Ge, C. Jin, M. Miao, Z. Jin, T. Gao, X. Jiang, P. Dai, Y. Bando, R. Li, J. Rong and X. Bin Wang, *J. Mater. Chem. A*, 2022, **10**, 846–854.
151 F. Liu, Q. Zhou, Y. Li and J. Pang, *Nanomaterials*, 2022, **12**, 318.
152 C. Yang, D. Bu and S. Huang, *Ceram. Int.*, 2022, **48**, 27658–27663.
153 Y. Sun, J. Bian and Q. Zhu, *J. Mol. Liq.*, 2022, **349**, 118216.
154 B. Isik, V. Ugraskan, F. Cakar and O. Yazici, *Res. Chem. Intermed.*, 2022, **48**, 4249–4268.
155 J. Li, M. Xia, L. Zhang, J. Tao, C. Wang and T. Wu, *Funct. Mater. Lett.*, 2021, **15**, 2251009.
156 G. Lian, X. Zhang, S. Zhang, D. Liu, D. Cui and Q. Wang, *Energy Environ. Sci.*, 2012, **5**, 7072–7080.
157 S. A. Sassman and L. S. Lee, *Environ. Sci. Technol.*, 2005, **39**, 7452–7459.
158 A. Sapkota, A. R. Sapkota, M. Kucharski, J. Burke, S. McKenzie, P. Walker and R. Lawrence, *Environ. Int.*, 2008, **34**, 1215–1226.
159 V. Gadore, S. Ranjan Mishra and M. Ahmaruzzaman, *Chem. Eng. J.*, 2023, **475**, 146157.
160 T. Heberer, *Toxicol. Lett.*, 2002, **131**, 5–17.
161 B. Halling-Sørensen, S. Nors Nielsen, P. F. Lanzky, F. Ingerslev, H. C. Holten Lützhøft and S. E. Jørgensen, *Chemosphere*, 1998, **36**, 357–393.
162 P. Grenni, V. Ancona and A. Barra Caracciolo, *Microchem. J.*, 2018, **136**, 25–39.
163 T. A. Ternes, *Water Res.*, 1998, **32**, 3245–3260.
164 K. Kümmerer, *Chemosphere*, 2001, **45**, 957–969.
165 W. Yang, Y. Wu, L. Zhang, J. Jiang and L. Feng, *Desalin. Water Treat.*, 2015, **54**, 1134–1140.
166 S. R. Mishra, V. Gadore, R. Verma, K. R. B. Singh, J. Singh and M. Ahmaruzzaman, *Chem. Eng. J.*, 2023, 146207.
167 J. Gomes, R. Costa, R. M. Quinta-Ferreira and R. C. Martins, *Sci. Total Environ.*, 2017, **586**, 265–283.
168 Y. Chao, W. Zhu, J. Chen, P. Wu, X. Wu, H. Li, C. Han and S. Yan, *Green Chem. Lett. Rev.*, 2014, **7**, 330–336.
169 Z. Liu, K. Zhao, D. Li and Y. Tang, *J. Am. Ceram. Soc.*, 2021, **104**, 1601–1610.
170 Y. Chao, J. Zhang, H. Li, P. Wu, X. Li, H. Chang, J. He, H. Wu, H. Li and W. Zhu, *Chem. Eng. J.*, 2020, **387**, 124138.

171 N. Lv, L. Sun, L. Chen, Y. Li, J. Zhang, P. Wu, H. Li, W. Zhu and H. Li, *Phys. Chem. Chem. Phys.*, 2019, **21**, 21867–21874.
172 D. Liu, W. Lei, S. Qin, K. D. Klika and Y. Chen, *Phys. Chem. Chem. Phys.*, 2015, **18**, 84–88.
173 G. Liu, Z. Zhang, C. Yan, Y. Wang, X. Ma, P. Gao and Y. Feng, *Chemosphere*, 2018, **207**, 534–542.
174 Q. Song, J. Liang, Y. Fang, C. Cao, Z. Liu, L. Li, Y. Huang, J. Lin and C. Tang, *J. Hazard. Mater.*, 2019, **364**, 654–662.
175 Q. Song, J. Liang, Y. Fang, Z. Guo, Z. Du, L. Zhang, Z. Liu, Y. Huang, J. Lin and C. Tang, *Chem. Eng. J.*, 2020, **394**, 124985.
176 L. Han, A. M. E. Khalil, J. Wang, Y. Chen, F. Li, H. Chang, H. Zhang, X. Liu, G. Li, Q. Jia and S. Zhang, *Sep. Purif. Technol.*, 2021, **278**, 119605.
177 Y. Guo, C. Yan, P. Wang, L. Rao and C. Wang, *Chem. Eng. J.*, 2020, **387**, 124136.
178 Y. Chao, B. Tang, J. Luo, P. Wu, D. Tao, H. Chang, X. Chu, Y. Huang, H. Li and W. Zhu, *J. Colloid Interface Sci.*, 2021, **584**, 154–163.
179 B. Wang, W. Bai, G. Wang, K. Guo, H. Duan, Y. Xue and C. Tang, *Colloids Surf., A*, 2022, **632**, 127749.
180 N. S. Mishra, S. Chandra and P. Saravanan, *J. Mol. Liq.*, 2023, **369**, 120969.
181 A. M. E. Khalil, L. Han, I. Maamoun, T. A. Tabish, Y. Chen, O. Eljamal, S. Zhang, D. Butler and F. A. Memon, *Adv. Sustainable Syst.*, 2022, **6**, 2200016.
182 E. Omrani, A. Ahmadpour, M. Heravi and T. R. Bastami, *Journal of Water Process Engineering*, 2022, **47**, 102581.
183 A. Goyal, D. Aggarwal, S. Kapoor, N. Goel, S. Singhal and J. Shukla, *New J. Chem.*, 2020, **44**, 3985–3997.
184 Q. Song, Y. Fang, Z. Liu, L. Li, Y. Wang, J. Liang, Y. Huang, J. Lin, L. Hu, J. Zhang and C. Tang, *Chem. Eng. J.*, 2017, **325**, 71–79.
185 L. J. Zhou, G. G. Ying, J. L. Zhao, J. F. Yang, L. Wang, B. Yang and S. Liu, *Environ. Pollut.*, 2011, **159**, 1877–1885.
186 J. Lu, Y. Ji, J. M. Chovelon and J. Lu, *Water Res.*, 2021, **198**, 117136.
187 J. Gibs, H. A. Heckathorn, M. T. Meyer, F. R. Klapinski, M. Alebus and R. L. Lippincott, *Sci. Total Environ.*, 2013, **458–460**, 107–116.
188 S. Raha, D. Mohanta and M. Ahmaruzzaman, *Sci. Rep.*, 2021, **11**, 1–19.
189 A. Pruden, R. Pei, H. Storteboom and K. H. Carlson, *Environ. Sci. Technol.*, 2006, **40**, 7445–7450.
190 J. Cai, J. Huang, S. Wang, J. Iocozzia, Z. Sun, J. Sun, Y. Yang, Y. Lai and Z. Lin, *Adv. Mater.*, 2019, **31**, 1806314.
191 Y. Wang, B. Jing, F. Wang, S. Wang, X. Liu, Z. Ao and C. Li, *Water Res.*, 2020, **180**, 115925.
192 M. Ahmaruzzaman and V. Gadore, *J. Environ. Chem. Eng.*, 2021, **9**, 105836.
193 S. R. Mishra and M. Ahmaruzzaman, *Mater. Today Commun.*, 2021, **28**, 102562.
194 L. Lin, Z. Yu and X. Wang, *Angew. Chem.*, 2019, **131**, 6225–6236.
195 C. Feng, L. Tang, Y. Deng, J. Wang, J. Luo, Y. Liu, X. Ouyang, H. Yang, J. Yu, J. Wang, C. Feng, L. Tang, J. Wang, J. Luo, Y. Liu, X. Ouyang, H. Yang, J. Yu and Y. Deng, *Green Chem. Lett. Rev.*, 2020, **30**, 2001922.
196 M. Ahmaruzzaman and S. R. Mishra, *Mater. Res. Bull.*, 2021, **143**, 111417.
197 F. Wang, Y. Feng, P. Chen, Y. Wang, Y. Su, Q. Zhang, Y. Zeng, Z. Xie, H. Liu, Y. Liu, W. Lv and G. Liu, *Appl. Catal., B*, 2018, **227**, 114–122.
198 Q. Xu, B. Zhu, B. Cheng, J. Yu, M. Zhou and W. Ho, *Appl. Catal., B*, 2019, **255**, 117770.
199 S. Angizi, S. A. A. Alem, M. Hasanzadeh Azar, F. Shayeganfar, M. I. Manning, A. Hatamie, A. Pakdel and A. Simchi, *Prog. Mater. Sci.*, 2022, **124**, 100884.
200 Y. Yang, C. Zhang, D. Huang, G. Zeng, J. Huang, C. Lai, C. Zhou, W. Wang, H. Guo, W. Xue, R. Deng, M. Cheng and W. Xiong, *Appl. Catal., B*, 2019, **245**, 87–99.
201 Y. Wu, X. Jin, H. Liu, W. Lv and G. Liu, *Sep. Purif. Technol.*, 2022, **303**, 122185.
202 S. Yu, X. Wang, H. Pang, R. Zhang, W. Song, D. Fu, T. Hayat and X. Wang, *Chem. Eng. J.*, 2018, **333**, 343–360.
203 L. Liang, S. Gao, J. Zhu, L. Wang, Y. Xiong, X. Xia and L. Yang, *Chem. Eng. J.*, 2020, **391**, 123599.
204 Z. Balta and E. B. Simsek, *J. Alloys Compd.*, 2022, **898**, 162897.
205 T. Yan, Z. Du, J. Wang, H. Cai, D. Bi, Z. Guo, Z. Liu, C. Tang and Y. Fang, *J. Alloys Compd.*, 2022, **894**, 162487.
206 Z. Du, L. Feng, Z. Guo, T. Yan, Q. Hu, J. Lin, Y. Huang, C. Tang and Y. Fang, *J. Colloid Interface Sci.*, 2021, **589**, 545–555.
207 Y. He, N. Xu, L. B. Junior, X. Hao, B. Yao, Q. Yang, D. Liu and Z. Ma, *Appl. Surf. Sci.*, 2020, **520**, 146336.
208 S. Sayegh, F. Tanos, A. Nada, G. Lesage, F. Zaviska, E. Petit, V. Rouessac, I. Iatsunskyi, E. Coy, R. Viter, D. Damberga, M. Weber, A. Razzouk, J. Stephan and M. Bechelany, *Dalton Trans.*, 2022, **51**, 2674–2695.
209 N. Liu, Y. Dang, B. Hu, M. Tian, H. Jiang, G. Quan, R. Qiao, J. Lei and X. Zhang, *Surf. Interfaces*, 2022, **35**, 102472.
210 H. He, W. Wang, C. Xu, S. Yang, C. Sun, X. Wang, Y. Yao, N. Mi, W. Xiang, S. Li and G. Liu, *Sci. Total Environ.*, 2020, **730**, 139100.
211 Z. Xiao, Y. Zheng, P. Chen, H. Liu, Z. Fang, J. Zhang, Z. Lin, Y. Zhang, J. Luo, W. Zhang, W. Lv and G. Liu, *Environ. Sci.: Nano*, 2022, **9**, 3110–3125.
212 X. Ji, X. Liu, Y. Guo and J. Zhang, *Chem. Eng. J.*, 2021, **425**, 131260.
213 B. Muthukutty, A. Krishnapandi and S. M. Chen, *New J. Chem.*, 2020, **44**, 2489–2499.
214 L. Lin, W. Jiang, M. Bechelany, M. Nasr, J. Jarvis, T. Schaub, R. R. Sapkota, P. Miele, H. Wang and P. Xu, *Chemosphere*, 2019, **220**, 921–929.
215 H. Cai, J. Wang, Z. Du, Z. Zhao, Y. Gu, Z. Guo, Y. Huang, C. Tang, G. Chen and Y. Fang, *Colloids Surf., A*, 2023, **663**, 131050.
216 B. Singh, K. Singh, M. Kumar, S. Thakur and A. Kumar, *Chem. Phys.*, 2020, **531**, 110659.
217 T. Han, Y. Chen and H. Shi, *Surf. Interfaces*, 2022, **35**, 102402.

218 P. Borthakur, P. K. Boruah and M. R. Das, *J. Environ. Chem. Eng.*, 2021, **9**, 104635.
219 S. A. Idrees, L. A. Jamil and K. M. Omer, *ACS Omega*, 2022, **7**, 37620–37628.
220 S. Mosleh, K. Dashtian, M. Ghaedi and M. Amiri, *RSC Adv.*, 2019, **9**, 30100–30111.
221 T. Sinha, M. Ahmaruzzaman and A. Bhattacharjee, *J. Environ. Chem. Eng.*, 2014, **2**, 2269–2279.
222 D. Wang, H. Shen, L. Guo, C. Wang and F. Fu, *ACS Omega*, 2016, **1**, 566–577.
223 Q. Liu, Y. Li, H. Chen, J. Lu, G. Yu, M. Möslang and Y. Zhou, *J. Hazard. Mater.*, 2020, **382**, 121040.
224 N. J. Ismail, M. H. D. Othman, R. Kamaludin, M. I. M. Esham, N. A. Ali, M. A. Rahman, J. Jaafar and S. A. Bakar, *Arabian J. Sci. Eng.*, 2019, **44**, 10031–10040.
225 H. Ouyang, H. Huang, H. Wang and X. Zheng, *J. Mater. Sci.*, 2020, **55**, 976–989.
226 V. Gadore, S. R. Mishra and M. Ahmaruzzaman, *J. Hazard. Mater.*, 2024, **461**, 132458.
227 P. Garcia-Muñoz, F. Fresno, V. A. de la Peña O'Shea and N. Keller, *Heterog. Photocatal.*, 2020, **378**, 107–162.
228 V. Gadore, S. R. Mishra and M. Ahmaruzzaman, *Environ. Sci. Pollut. Res.*, 2023, **30**, 90410–90457.
229 D. Mohanta, S. V. Gupta, V. Gadore, S. Paul and M. Ahmaruzzaman, *ACS Omega*, 2022, **7**, 20357–20368.
230 D. Gao, S. Zheng, L. Wang, C. Wang, H. Zhang and Q. Wang, *Sep. Purif. Technol.*, 2019, **224**, 308–314.
231 J. Diaz-Angulo, I. Gomez-Bonilla, C. Jimenez-Tohapanta, M. Mueses, M. Pinzon and F. Machuca-Martinez, *Photochem. Photobiol. Sci.*, 2019, **18**, 897.
232 E. Bae and W. Choi, *Environ. Sci. Technol.*, 2003, **37**, 147–152.
233 Y.-X. Li, X. Wang, C.-C. Wang, H. Fu, Y. Liu, P. Wang and C. Zhao, *J. Hazard. Mater.*, 2020, **399**, 123085.
234 S. Gao, T. Feng, C. Feng, N. Shang and C. Wang, *J. Colloid Interface Sci.*, 2016, **466**, 284–290.
235 C. Li, Y. Xu, W. Tu, G. Chen and R. Xu, *Green Chem.*, 2017, **19**, 882–899.
236 J. Qu, Q. Li, C. Luo, J. Cheng and X. Hou, *Coatings*, 2018, **8**, 214.
237 A. Pakdel, Y. Bando and D. Golberg, *Chem. Soc. Rev.*, 2014, **43**, 934–959.
238 Y. Guo, R. Wang, P. Wang, L. Rao and C. Wang, *ACS Appl. Mater. Interfaces*, 2018, **10**, 4640–4651.
239 Y. Guo, R. Wang, C. Yan, P. Wang, L. Rao and C. Wang, *Chemosphere*, 2019, **229**, 112–124.
240 X. Ji, Y. Guo, S. Hua, H. Li and S. Zhang, *New J. Chem.*, 2020, **44**, 9238–9247.
241 C. Cheng, W.-H. Fang, R. Long and O. V. Prezhdo, *JACS Au*, 2021, **1**, 550–559.
242 J. J. Guerard and Y. P. Chin, *J. Agric. Food Chem.*, 2012, **60**, 9801–9806.
243 H. Lee, J. Kim, D. Y. Kim and Y. Seo, *Org. Electron.*, 2018, **52**, 103–109.
244 Y. J. Jang, S. Thogiti, K. Y. Lee and J. H. Kim, *Crystals*, 2019, **9**, 452.
245 Y. Sheng, J. Yang, F. Wang, L. Liu, H. Liu, C. Yan and Z. Guo, *Appl. Surf. Sci.*, 2019, **465**, 154–163.
246 D. Liu, J. Song, J. S. Chung, S. H. Hur and W. M. Choi, *Molecules*, 2022, **27**, 6833.
247 R. V. Khose, K. D. Lokhande, M. A. Bhakare, P. S. Dhumal, P. H. Wadekar and S. Some, *ChemistrySelect*, 2021, **6**, 7956–7963.
248 M. Nasr, L. Soussan, R. Viter, C. Eid, R. Habchi, P. Miele and M. Bechelany, *New J. Chem.*, 2018, **42**, 1250–1259.
249 W. Liu and W. Hu, *Mater. Charact.*, 2022, **191**, 112165.
250 Q. P. Zhang, D. M. Liang, W. F. Zhu, J. H. Liu, Y. Wu, D. G. Xu, X. Y. Bai, M. Wei and Y. L. Zhou, *J. Solid State Chem.*, 2019, **269**, 594–599.
251 E. Erusappan, S. Thiripuranthagan, M. Durai, S. Kumaravel and T. Vembuli, *New J. Chem.*, 2020, **44**, 7758–7770.
252 U. Rafiq, M. Wahid and K. Majid, *ChemistrySelect*, 2020, **5**, 11637–11647.
253 W. Li, Y. Liu, J. Di, M. Ji, J. Xia and H. Li, *Phys. Status Solidi*, 2018, **215**, 1800146.
254 S. Sankeetha, R. Muralidharan, N. Abirami, H. Leelavathi, S. Tamizharasan, A. Kumarasamy and R. Arulmozhi, *Ceram. Int.*, 2023, **49**, 6125–6138.
255 Q. Zhang, W. Zhang, B. Liang, J. Liu, D. Lan and M. Jiao, *J. Inorg. Organomet. Polym. Mater.*, 2022, **32**, 4434–4440.
256 W. Wang, L. Song, H. Zhang, G. Zhang and J. Cao, *Front. Chem. Sci. Eng.*, 2021, **15**, 1537–1549.
257 A. ul Ahmad, A. Abbas, S. Ali, M. F. e-alam, Z. Farooq, Q. Abbas, M. Ahmad, A. Farid, A. Muhammad afzal, H. M. Umair Arshad, M. Javid and M. Iqbal, *Ceram. Int.*, 2021, **47**, 10089–10095.
258 A. Khalid, P. Ahmad, A. Khan, M. U. Khandaker, I. Kebaili, M. M. Alam, I. U. Din, S. Muhammad, Z. Razzaq, I. U. Rehman, H. A. Abbasi and D. Hayat, *RSC Adv.*, 2022, **12**, 6592–6600.
259 C. Jiang, S. J. A. Moniz, A. Wang, T. Zhang and J. Tang, *Chem. Soc. Rev.*, 2017, **46**, 4645–4660.
260 T. Yao, X. An, H. Han, J. Q. Chen and C. Li, *Adv. Energy Mater.*, 2018, **8**, 1800210.
261 J. Jia, L. C. Seitz, J. D. Benck, Y. Huo, Y. Chen, J. W. D. Ng, T. Bilir, J. S. Harris and T. F. Jaramillo, *Nat. Commun.*, 2016, **7**, 1–6.
262 A. Hossain, K. Sakthipandi, A. K. M. Atique Ullah and S. Roy, *Nano-Micro Lett.*, 2019, **11**, 1–26.
263 Z. He, J. Zhang, X. Li, S. Guan, M. Dai and S. Wang, *Small*, 2020, **16**, 2005051.
264 G. Zuo, Y. Wang, W. L. Teo, A. Xie, Y. Guo, Y. Dai, W. Zhou, D. Jana, Q. Xian, W. Dong and Y. Zhao, *Angew. Chem.*, 2020, **132**, 11383–11388.
265 Y. Li, B. Sun, H. Lin, Q. Ruan, Y. Geng, J. Liu, H. Wang, Y. Yang, L. Wang and K. Chiu Tam, *Appl. Catal., B*, 2020, **267**, 118702.
266 H. Si, G. Lian, J. Wang, L. Li, Q. Wang, D. Cui and C. P. Wong, *ACS Appl. Mater. Interfaces*, 2016, **8**, 1578–1582.
267 C. Gautam, C. S. Tiwary, S. Jose, G. Brunetto, S. Ozden, S. Vinod, P. Raghavan, S. Biradar, D. S. Galvao and P. M. Ajayan, *ACS Nano*, 2015, **9**, 12088–12095.

268 A. P. Farkas, Á. Szitás, D. Jurdi, K. Palotás, J. Kiss and Z. Kónya, *Appl. Catal., A*, 2020, **592**, 117440.
269 Y. Cao, R. Zhang, T. Zhou, S. Jin, J. Huang, L. Ye, Z. Huang, F. Wang and Y. Zhou, *ACS Appl. Mater. Interfaces*, 2020, **12**, 9935–9943.
270 X. Xing, M. Zhang, L. Hou, L. Xiao, Q. Li and J. Yang, *Int. J. Hydrogen Energy*, 2017, **42**, 28434–28444.
271 J. T. Grant, C. A. Carrero, F. Goeltl, J. Venegas, P. Mueller, S. P. Burt, S. E. Specht, W. P. McDermott, A. Chieregato and I. Hermans, *Science*, 2016, **354**, 1570–1573.
272 P. F. Sun, W. L. Wang, X. Zhao and J. S. Dang, *Phys. Chem. Chem. Phys.*, 2020, **22**, 22627–22634.
273 M. N. Ivanova, Y. A. Vorotnikov, E. E. Plotnikova, M. V. Marchuk, A. A. Ivanov, I. P. Asanov, A. R. Tsygankova, E. D. Grayfer, V. E. Fedorov and M. A. Shestopalov, *Inorg. Chem.*, 2020, **59**, 6439–6448.
274 M. S. Meera, S. K. Sasidharan, A. Hossain, J. Kiss, Z. Konya, L. Elias and S. M. A. Shibli, *ACS Appl. Energy Mater.*, 2022, **5**, 3578–3586.
275 A. Pendse, S. Cetindag, M. H. Lin, A. Rackovic, R. Debbarma, S. Almassi, B. P. Chaplin, V. Berry, J. W. Shan and S. Kim, *Small*, 2019, **15**, 1904590.
276 X. Wen, Y. Wang and J. Zhao, *New J. Chem.*, 2018, **42**, 12838–12844.
277 J. Peng, S. Wang, P. H. Zhang, L. P. Jiang, J. J. Shi and J. J. Zhu, *J. Biomed. Nanotechnol.*, 2013, **9**, 1679–1685.
278 S. Meng, X. Ye, X. Ning, M. Xie, X. Fu and S. Chen, *Appl. Catal., B*, 2016, **182**, 356–368.
279 X. Xiao, D. Huang, Y. Fu, M. Wen, X. Jiang, X. Lv, M. Li, L. Gao, S. Liu, M. Wang, C. Zhao and Y. Shen, *ACS Appl. Mater. Interfaces*, 2018, **10**, 4689–4696.
280 M. Tahir, *Energy Fuels*, 2021, **35**, 14197–14211.
281 J. C. Wang, Y. Hou, F. D. Feng, W. X. Wang, W. Shi, W. Zhang, Y. Li, H. Lou and C. X. Cui, *Appl. Surf. Sci.*, 2021, **537**, 148014.
282 S. Thaweesak, S. Wang, M. Lyu, M. Xiao, P. Peerakiatkhajohn and L. Wang, *Dalton Trans.*, 2017, **46**, 10714–10720.
283 B. Wahbeh, T. A. Hamed and R. Kasher, *Renewable Energy*, 2012, **48**, 10–15.
284 Q. Liu, C. Chen, M. Du, Y. Wu, C. Ren, K. Ding, M. Song and C. Huang, *ACS Appl. Nano Mater.*, 2018, **1**, 4566–4575.
285 D. P. Kumar, J. Choi, S. Hong, D. A. Reddy, S. Lee and T. K. Kim, *ACS Sustain. Chem. Eng.*, 2016, **4**, 7158–7166.
286 T. C. Bhagya, A. Krishnan, S. Arunima Rajan, M. Ameen Sha, B. R. Sreelekshmy, P. Jineesh and S. M. A. Shibli, *Photochem. Photobiol. Sci.*, 2019, **18**, 1716–1726.
287 G. J. Lee, Y. H. Hou, C. Y. Chen, C. Y. Tsay, Y. C. Chang, J. H. Chen, T. L. Horng, S. Anandan and J. J. Wu, *Int. J. Hydrogen Energy*, 2021, **46**, 5938–5948.
288 S. Mao, J. W. Shi, G. Sun, Y. Zhang, X. Ji, Y. Lv, B. Wang, Y. Xu and Y. Cheng, *Chem. Eng. J.*, 2021, **404**, 126533.
289 A. Sarilmaz, G. Yanalak, E. Aslan, F. Ozel, I. H. Patir and M. Ersoz, *Renewable Energy*, 2021, **164**, 254–259.
290 A. Merlo, V. R. S. S. Mokkapati, S. Pandit and I. Mijakovic, *Biomater. Sci.*, 2018, **6**, 2298–2311.
291 S. M. Sharker, *Int. J. Nanomed.*, 2019, **14**, 9983.